

DAMAGE IN DUAL PHASE STEELS UNDER INDUSTRIAL FORMING
CONDITIONS

A THESIS SUBMITTED TO
THE GRADUATE SCHOOL OF NATURAL AND APPLIED SCIENCES
OF
MIDDLE EAST TECHNICAL UNIVERSITY

BY

MERVE OBANOĐLU

IN PARTIAL FULFILLMENT OF THE REQUIREMENTS
FOR
THE DEGREE OF MASTER OF SCIENCE
IN
METALLURGICAL AND MATERIALS ENGINEERING

NOVEMBER 2019

Approval of the thesis:

**DAMAGE IN DUAL PHASE STEELS UNDER INDUSTRIAL FORMING
CONDITIONS**

submitted by **MERVE ÇOBANOĞLU** in partial fulfillment of the requirements for
the degree of **Master of Science in Metallurgical and Materials Engineering**
Department, Middle East Technical University by,

Prof. Dr. Halil Kalıpçılar
Dean, Graduate School of **Natural and Applied Sciences**

Prof. Dr. Cemil Hakan Gür
Head of Department, **Met. and Mat. Eng.**

Assoc. Prof. Dr. Mert Efe
Supervisor, **Met. and Mat. Eng., METU**

Examining Committee Members:

Prof. Dr. Bilgehan Ögel
Met. and Mat. Eng., METU

Assoc. Prof. Dr. Mert Efe
Met. and Mat. Eng., METU

Prof. Dr. Cemil Hakan Gür
Met. and Mat. Eng., METU

Assoc. Prof. Dr. Caner Şimşir
Met. and Mat. Eng., METU

Assist. Prof. Dr. Eda Aydoğan Güngör
Integrated Manufacturing Research and Application Center,
Sabancı University

Date: 22.11.2019

I hereby declare that all information in this document has been obtained and presented in accordance with academic rules and ethical conduct. I also declare that, as required by these rules and conduct, I have fully cited and referenced all material and results that are not original to this work.

Name, Surname: Merve obanođlu

Signature:

ABSTRACT

DAMAGE IN DUAL PHASE STEELS UNDER INDUSTRIAL FORMING CONDITIONS

Çobanoğlu, Merve
Master of Science , Metallurgical and Materials Engineering
Supervisor: Assoc. Prof. Dr. Mert Efe

November 2019, 71 pages

Dynamic strain aging (DSA) is an undesirable mechanism that affects the deformation of dual-phase (DP) steels. In the first part of this thesis, the DSA behavior was studied with tensile tests coupled with digital image correlation (DIC) technique. Strain maps revealed band-type strain localizations under the DSA conditions, which were similar to PLC-type of banding. After the tensile tests, fracture surfaces were investigated by electron microscopy, and the fracture behavior has changed with different test conditions. In the second part, the relation between DSA and damage in DP steels were investigated through tensile tests that were designed to reveal the changes in elastic modulus. The damage parameter was measured and compared under quasi-static and industrial deformation conditions (temperatures: 25 vs. 200, 300 °C and strain rates: 10^{-3} vs. 10 s^{-1}) for DP590 and DP800 steels. At a given strain, the damage values can be up to 700% higher at industrial forming conditions, under which dynamic strain aging (DSA) controls the deformation behavior. Measured damage parameters were also confirmed with the void fraction characterization by microscopy, which also provided details on the void shape and distribution with respect to the deformation conditions.

Keywords: Damage, Dual – Phase (DP), Void, Forming, Aging

ÖZ

ÇİFT FAZLI ÇELİKLERDE ENDÜSTRİYEL ŞEKİLLENDİRİLME KOŞULLARINDA HASAR OLUŞUMU

Çobanoğlu, Merve
Yüksek Lisans, Metalurji ve Malzeme Mühendisliği
Tez Danışmanı: Doç. Dr. Mert Efe

Kasım 2019, 71 sayfa

Dinamik gerilme yaşlanması (DGY), DP çeliklerinin deformasyonunu etkileyen istenmeyen bir mekanizmadır. Bu tezin ilk bölümünde, DGY davranışı dijital görüntü ilişkilendirme (DGI) tekniği ile birleştirilmiş çekme testleri ile incelenmiştir. Gerinim haritaları, DGY koşullarında, PLC-tipi bantlara benzer olan bant şeklinde gerinim lokalleşmelerini ortaya çıkarmıştır. Çekme testlerinden sonra, kırık yüzeyler elektron mikroskopuyla incelenmiş ve farklı test koşullarında kırılma davranışının değiştiği görülmüştür. İkinci bölümde, DP çeliklerinde DGY ve hasar arasındaki ilişki, elastik katsayıdaki değişimi ortaya çıkartmak için tasarlanmış çekme testleri ile incelenmiştir. Hasar parametreleri DP590 ve DP800 çelikleri için, kuazi-statik ve endüstriyel şekillendirme koşullarında (sıcaklık: 25 vs 200, 300 °C and gerinim hızları: 10^{-3} vs 10 s⁻¹) ölçülmüş ve karşılaştırılmıştır. Belirli bir gerilimde, hasar değerleri, dinamik gerinim yaşlanmasının (DGY) deformasyon davranışını kontrol ettiği endüstriyel şekillendirme koşulları için %700'e kadar daha yüksek olabilir. Ölçülen hasar parametresi değerleri, mikroskop yardımıyla karakterize edilen boşlukların yüzdesi ile doğrulanmıştır, ayrıca şekillendirme koşullarına göre boşlukların şekli ve dağılımı hakkında ayrıntılı bilgi sağlanmıştır.

Anahtar Kelimeler: Hasar, Çift – Fazlı Çelikler, Şekillendirilebilirlik, Yaşlanma

To my beloved parents...

ACKNOWLEDGEMENTS

The Scientific Research Council of Turkey- TÜBİTAK supported this work, Grants No: 115M642 and 218M556.

Firstly, I am deeply indebted to my advisor Assoc. Prof. Dr. Mert EFE for his patient guidance and enthusiastic encouragement. He always shares his knowledge and experience with me whenever I got stuck during this study. It would be impossible to complete my master's degree without his support. I wish him all the best in the new chapter of his life in the U.S. I would also like to thank Assoc. Prof. Dr. Caner ŞİMŞİR for his valuable and constructive advices. I feel very lucky knowing his support behind me.

I also wish to thank my labmates, Berkay BAYRAMİN, Baran GÜLER, Mustafa BALCILAR, and especially Orhan Berk AYTUNA, for all his kindness and help in SEM images. I also would like to thank Dr. Osman El-Atwani to visit our lab and share his experience with us. I feel fortunate to have a chance to work with him. I would like to express my appreciation to MSc. Tuğçe KALELİ who willingly helped me for the ultrasonic sound velocity measurements and Dr. Süha TİRKEŞ, who is always ready to help whenever I needed. I am thankful to Rasim Köksal ERTAN, Yasin DEMIRKOL, Yahya TUNÇ and Heval DEMIRCI, who are the staff of Metal Forming Center of Excellence for their help in tensile tests.

I especially thank my best friends, Ece USLU, for all her support with her friendship in all my academic and social life since my undergraduate education and Baturalp GONCAGÜL, who is always supportive and making me laugh whatever happen in life. I am also grateful to my colleagues and friends Çağrı ÖZDİLEK, Didem MİMİROĞLU, Çağatay Mert ORAL, and Şeniz YAMAN.

Special thanks to Duygu Sezen POLAT and Cansu BALKU, who are sisters from another mother. I am sure that they will be there for me not only today but also in the future.

Last but not least, I dedicated this work to my parents, Elif and Murat OBANOĐLU for the most meaningful support. I am always sure that they are my best supporters and always on my side, whatever my decision is. Many thanks to my sisters Melek OBANOĐLU and Gölce OBANOĐLU, and my lovely cat Korsan.

TABLE OF CONTENTS

ABSTRACT	v
ÖZ	vii
ACKNOWLEDGEMENTS.....	x
TABLE OF CONTENTS	xii
LIST OF TABLES.....	xiv
LIST OF FIGURES	xvi
1. INTRODUCTION.....	1
2. LITERATURE REVIEW.....	5
2.1. DP Steels.....	5
2.2. Mechanical Properties of DP Steels.....	9
2.3. Forming of DP Steels.....	11
2.4. Dynamic Stain Aging in DP Steels.....	14
2.5. Damage in DP Steels.....	17
2.6. Main Findings and Gaps in Literature	19
3. MATERIALS AND METHODS	21
3.1. Materials.....	21
3.2. Digital Image Correlation (DIC) Tests	21
3.2.1. Digital Image Correlation (DIC) Technique and Sample Preparation	22
3.2.2. Digital Image Correlation (DIC) Tensile Tests and Experimental Setup	22
3.2.3. Digital Image Correlation (DIC) Program and Strain Maps	25
3.3. Microstructural Analysis.....	26
3.3.1. Scanning Electron Microscope (SEM) Images	26

3.4. Damage Analysis.....	27
3.4.1. Tensile Tests for Damage	27
3.4.2. Stain Measurements	30
3.4.3. Elastic Modulus and Damage Parameter Measurement	32
4. RESULT AND DISCUSSION	35
4.1. Macro DIC analysis of DP steels.....	35
4.1.1. DIC Results of DP590	35
4.1.2. DIC Results of DP800	41
4.2. Fracture Analysis of DP Steels.....	44
4.2.1. Fracture Analysis of DP590.....	45
4.2.2. Fracture Analysis of DP800.....	48
4.3. Damage Parameter Evolution with Temperature and Strain Rate.....	50
4.4. Microstructural Analysis of Damage.....	59
5. CONCLUSIONS and FUTURE WORKS.....	63
5.1. Conclusions	63
5.2. Future Works	65
REFERENCES.....	67

LIST OF TABLES

TABLES

Table 2.1 Alloying elements with their properties [14]	7
Table 3.1 Chemical compositions of DP590 and DP800.....	21
Table 3.2 Experimental matrix of DIC tensile tests.....	23
Table 3.3 Experiment matrix of tensile tests for damage analysis.....	29
Table 3.4 Experimental matrix with the targeted and measured strain values	31
Table 3.5 Comparison of RFDA and USVM damage measurements for deformed DP800 samples	34
Table 4.1 Damage parameter and E modulus values of DP590 at RT and 10^{-3} s^{-1} ...	52
Table 4.2 Damage parameter and E modulus values of DP590 at 200° C and 10^{-3} s^{-1}	52
Table 4.3 Damage parameter and E modulus values of DP590 at 300° C and 10^{-3} s^{-1}	52
Table 4.4 Damage parameter and E modulus values of DP590 at RT and 10 s^{-1}	53
Table 4.5 Damage parameter and E modulus values of DP590 at 200° C and 10 s^{-1}	53
Table 4.6 Damage parameter and E modulus values of DP590 at 300° C and 10 s^{-1}	53
Table 4.7 Damage parameter and E modulus values of DP800 at RT and 10^{-3} s^{-1} ...	56
Table 4.8 Damage parameter and E modulus values of DP800 at 200° C and 10^{-3} s^{-1}	56
Table 4.9 Damage parameter and E modulus values of DP800 at 300° C and 10^{-3} s^{-1}	56
Table 4.10 Damage parameter and E modulus values of DP800 at RT and 10 s^{-1} ...	56
Table 4.11 Damage parameter and E modulus values of DP800 at 200° C and 10 s^{-1}	57

Table 4.12 Damage parameter and E modulus values of DP800 at 300° C and 10 s⁻¹
.....57

Table 4.13 Average void sizes and volume fractions in DP590 & DP800 obtained
from SEM pictures. Damage parameters are also provided for comparison.62

LIST OF FIGURES

FIGURES

Figure 1.1 Skeleton of different cars; a)2017 Jeep Renegade[1], b)2010 Volvo S60[2], c)2016 Honda Civic[3], d)2016 Lincoln Continental[4] with their using materials ...	1
Figure 2.1 Different examples given as a pie chart; a) The usage of DP steels in Generals Motors autos throughout the years. b)2015 model Ford Edge [1]	6
Figure 2.2 Schematic view of the car skeleton produced from different DP steel grades of SAAB [15].....	6
Figure 2.3 Microstructure images of a)DP590, b)DP800 as received condition.....	7
Figure 2.4 Heat treatment processes to observe Dual-Phase steels [14]	8
Figure 2.5 Comparison of the mechanical properties of Dual Phase Steels with others [28], [29].....	10
Figure 2.6 Absorbed energy vs. Stress graph of the different types of steels [33] ...	12
Figure 2.7 Jaoul-Crussard analysis graph of typical DP steel is given with the strain hardening stages [34].....	13
Figure 2.8 TEM images of the DP steel at different stages and strain values; a)1% strain, dislocation tangles, b)2% strain, already formed dislocation cell structure, c)7% strain, dislocation cells in ferrite, d)14% strain, dislocation cells in ferrite [34].....	14
Figure 2.9 Stress strain graph of DP590 observed after tensile tests at different strain rates and temperature (DSA range) [8].....	17
Figure 2.10 Stress strain graph of DP800 observed after tensile tests at different strain rates and temperature (DSA range) [8].....	17
Figure 3.1 TA-BAEHR DIL805A/D-Deformation Dilatomete.....	21
Figure 3.2 Technical drawing of the DIC testing specimen using in TA-BAEHR DIL805A/D-Deformation Dilatometer. Dimensions are in millimeter.	23
Figure 3.3 a) TA-BAEHR DIL805A/D horizontal induction coil; b) K type thermocouple i.e. suitable for dilatometer	24

Figure 3.4 Spot welding device for thermocouple welding to sample for temperature control of dilatometer	24
Figure 3.5 Thermocouple welded sample placed in dilatometer	24
Figure 3.6 Experimental setup (Camera assembly with a tripod placed perpendicular to the sample)	25
Figure 3.7 Technical drawing of the testing specimen.....	27
Figure 3.8 Gleeble 3500 device.....	28
Figure 3.9 Tensile test sample located in the Gleeble the chamber before test	28
Figure 3.10 Samples a)after tested preparing for the Argus analysis, located with the help of Argus apparatus; b) photos were taken for the analysis; c) Argus analysis started based on the taken photos.....	30
Figure 3.11 Argus analysis results of three different samples (DP590, 10 s-1 strain rate, 300 °C) tested at target strain values of 2%, 8%, 16% (from left to right).....	32
Figure 4.1 DP590 RT 10 ⁻³ s ⁻¹ ; a)5%, b)10%, c)20% [before neck], d)23% neck strain, DIC analysis	36
Figure 4.2 DP590 RT s ⁻¹ ; a)5%, b)6.7%, c)8.65%, d)10.7%, e)14.1%, f)16.4%, g)18.8% (neck) strain, DIC analysis	36
Figure 4.3 DP590 200°C 10 ⁻³ s ⁻¹ ; a)5%, b)10%, c)20% [before neck], d)24% neck strain, DIC analysis	37
Figure 4.4 DP590 200 °C s ⁻¹ ; a)5%, b)9.1%, c)10.4%, d)11.6%, e)13.02%, f)14.5%, g)16%, h)18.3%(neck) strain, DIC analysis	37
Figure 4.5 Stress&Strain curves of the DIC analyzed DP590 samples observed from tensile tests	38
Figure 4.6 DP590 RT 10 ⁻³ s ⁻¹ ; a) 5%, b) 10%; DP590 RT 1 s ⁻¹ ;a) 5%, c) 10%, d) 11% strain DIC analysis	39
Figure 4.7 DP590 200 °C 10 ⁻³ s ⁻¹ ; a) 5%, b) 10%; DP590 200 °C 1 s ⁻¹ ; a) 5%, c) 10%, d) 11% strain, DIC analysis	39
Figure 4.8 DP800 RT 10 ⁻³ s ⁻¹ ; a)5%, b)10%, c)13% [before neck], d)14% neck strain, DIC analysis	41

Figure 4.9 DP800 RT 1 s^{-1} ; a)3%, b)4%, c)5.2%, d)6.45%, e)7.8%, f)9.2%, g)14.6% (neck) strain, DIC analysis	42
Figure 4.10 DP800 $200^\circ\text{C } 10^{-3} \text{ s}^{-1}$; a)5%, b)10%, c) 17%, d)20% strain, DIC analysis	42
Figure 4.11 DP800 $200^\circ\text{C } 1 \text{ s}^{-1}$; a)3%, b)4%, c)5.2%, d)6.45%, e)7.8% strain, DIC analysis	43
Figure 4.12 Stress&Strain curves of the DIC analyzed DP800 samples observed from tensile tests.....	43
Figure 4.13 Fracture surface of DP590 10^{-3} s^{-1} ; a)RT, b)200 °C (red circles shows the nucleation cites)	45
Figure 4.14 Fracture surface of DP590 1 s^{-1} RT	46
Figure 4.15 Fracture surface of DP590 1 s^{-1} 200 °C; a)3000x, b)3000x, c)1600x, d)1500x	47
Figure 4.16 Fracture surface of DP800 10^{-3} s^{-1} RT.....	49
Figure 4.17 Fracture surface of DP800 1 s^{-1} RT	49
Figure 4.18 Damage parameter vs. strain graphs of DP590 tested at different temperatures; (top) low strain rate, 10^{-3} s^{-1} vs (bottom) high strain rate, 10 s^{-1}	54
Figure 4.19 Damage parameter vs. strain graphs of DP800 tested at different temperatures; (top) low strain rate, 10^{-3} s^{-1} vs (bottom) high strain rate, 10 s^{-1}	58
Figure 4.20 Damage parameter vs. temperature graph of DP590 and DP800 at 10^{-3} s^{-1} and 10 s^{-1} strain rates, and at their uniform strains (16% and 10%).	59
Figure 4.21 SEM pictures of DP590 tested at; a) 10^{-3} s^{-1} - RT, b) 10 s^{-1} - RT, c) 10 s^{-1} - 300°C , and at same strain of 16 %. Scale bars are $30 \mu\text{m}$	60
Figure 4.22 SEM pictures of DP800 tested at; a) 10^{-3} s^{-1} - RT, b) 10 s^{-1} - RT, c) 10 s^{-1} - 300°C , and at same strain of 10 %. Scale bars are $30 \mu\text{m}$	61

CHAPTER 1

INTRODUCTION

Dual-phase steels are the most used materials in today's automotive industry, nearly 50% of the vehicle's structural parts comprise of DP steels (Fig. 1) [1]–[4], [5]. Increasing use of DP steels has promoted the studies to understand the deformation behavior of these steels during the forming process [6]. In the automotive industry, certain forming processes require large strains ($\epsilon > 0.1$) and high strain rates ($\dot{\epsilon} > 1 \text{ s}^{-1}$). Combined together, these deformation parameters also cause heating of the workpieces ($T > 100 \text{ }^\circ\text{C}$). Although DP steels have ideal mechanical properties, they are limited in these processes because of relatively low fracture strains [7].

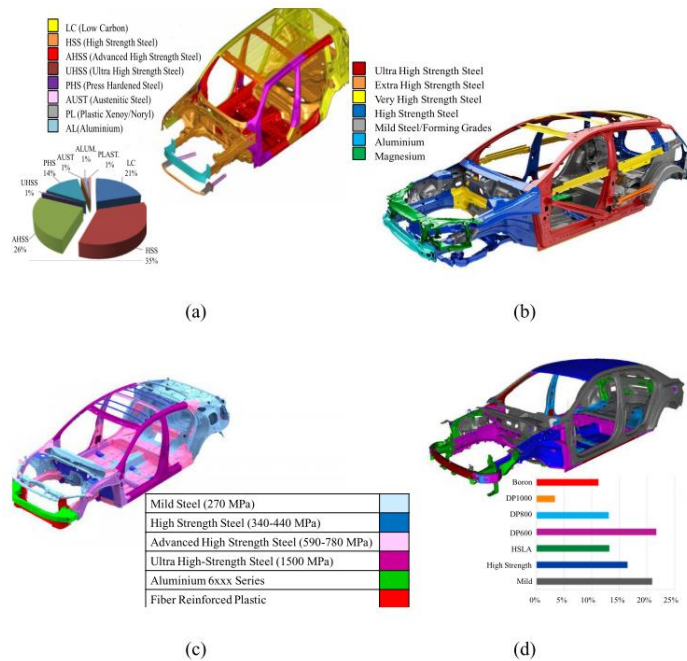


Figure 1.1 Skeleton of different cars; a)2017 Jeep Renegade[1], b)2010 Volvo S60[2], c)2016 Honda Civic[3], d)2016 Lincoln Continental[4] with their using materials

DP steels suffer from lowered ductility and negative strain rate sensitivity under the deformation conditions relevant to the forming processes. According to the several studies in the literature, dynamic strain aging is the leading factor responsible from the lower formability of dual-phase steels [8]–[10]. The DSA activity is higher in DP590 steel with respect to DP800 due to the increased ferrite content, which reflects itself in reduced uniform and total ductility at relatively high temperatures and strain rates ($200 < T < 300$ °C and $0.1 < \dot{\epsilon} < 1$ s⁻¹) [8]. On the other hand, the effects of these thermo-mechanical parameters on the damage evolution have not been investigated in the literature.

The damage mechanisms in dual-phase materials are especially complicated compared to the single-phase materials [11] , [12]. Dual-phase steels are sensitive to damage because of strain mismatch between ferrite and martensite phases. Since martensite is a brittle phase, damage formation is relatively easy for DP steels [13], [14]. Understanding the relationship between the DSA and damage evolution will help to get rid of limitations during industrial forming processes, as well as to maintain some critical mechanical and physical properties of the material such as hardness, density, elastic modulus, yield strength, etc. in service conditions [15]–[17].

In this study, DSA controlled deformation behavior was examined with DIC technique in two different grades of dual-phase steels (DP590 and DP800). Due to observed flow instabilities in tensile tests and strain localizations at strain maps, it was decided to investigate the fracture surface of these samples to get more information. Although typical ductile fracture characterization seen at both grades and all parameters, some differences observed at the DSA range. Therefore, it was decided to study damage mechanism for the DSA range in the DP steels, which is the major topic of this thesis. The evolution of damage parameter in two different grades of dual-phase steels (DP590 and DP800) was evaluated from the uniaxial tensile tests which were conducted at three different temperatures (RT, 200 °C and 300 °C) and two different strain rates (10^{-3} s⁻¹ and 10 s⁻¹). These conditions were selected in accordance with the previous studies and considering the industrial forming conditions, where DSA

controlled the deformation behavior and resulted in lower formability. The main aim was to test the effects of DSA on the damage evolution by comparing the low temperature and strain-rate deformation behavior with the DSA-controlled one.

CHAPTER 2

LITERATURE REVIEW

2.1. DP Steels

Steels are the most valuable structural materials used in many areas of life, especially in the automotive industry. Significant research has been done to improve car safety in case of crash, and fuel efficiency, resulting in the production of advanced high-strength steels (AHSS) [14]. Dual-phase (DP) steels are the most prominent and widely used members of the AHSS family [5]. These steels are the great combination of strength and toughness; they consist of two phases i.e., martensite and ferrite. Martensite provides high strength; meanwhile, ferrite provides ductility [14]. Compared to the traditional plain carbon steels, DP steels have many advantages such as excellent mechanical properties (higher strength, higher ductility, toughness), higher durability and long fatigue life, etc. [19].

Due to these properties, DP steels are not only preferred today but also will be preferred in the future are preferred for the production of automobiles [5]. Different examples are given in the following figures that show the usage of DP steels in the car manufacturing application [5], [20].

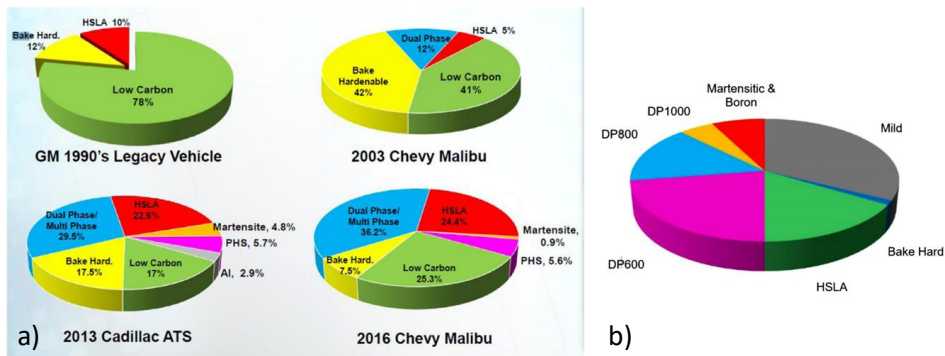


Figure 2.1 Different examples given as a pie chart; a) The usage of DP steels in Generals Motors autos throughout the years. b)2015 model Ford Edge [1]

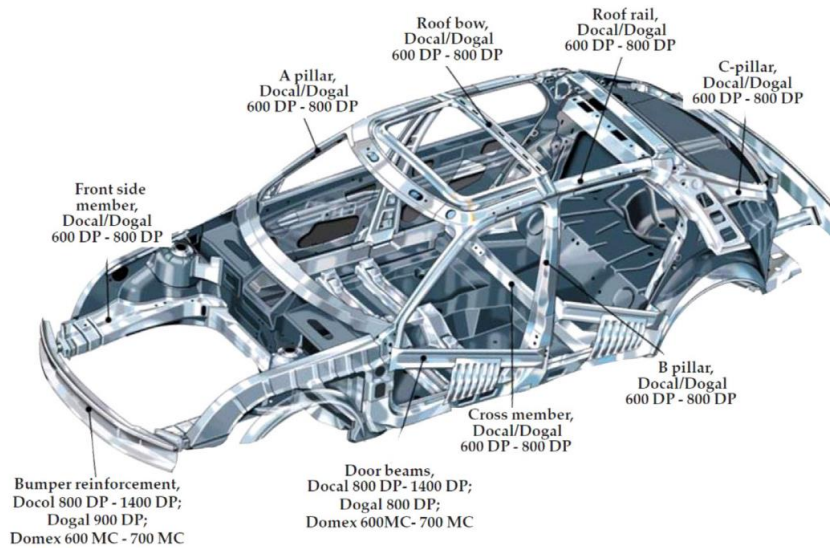


Figure 2.2 Schematic view of the car skeleton produced from different DP steel grades of SAAB [15]

Similar to the other steels, carbon is the primary alloying element of the DP steels. They generally contain 0.06 - 0.15 weight percent carbon. In order to attain the required microstructures, other alloying elements are also used as an additive, such as Mn, Cr, Mo, Si, V, and Nb [14]. The contributions of these alloying elements to the steel are given in the following table.

Table 2.1 Alloying elements with their properties [14]

Alloying Element	Property
C, Mn	Austenite stabilizers, strength martensite, cause SS strengthening in ferrite
Cr, Mo	Retard pearlite (or bainite) formation
Si	Promote ferrite transformation
V, Nb	Promote precipitation strengthening and microstructure refinement

The chemical composition and amount of alloying elements of the steels used in this thesis are given in the material section. As received microstructures of DP590 and DP800 given in the figure 2.3.

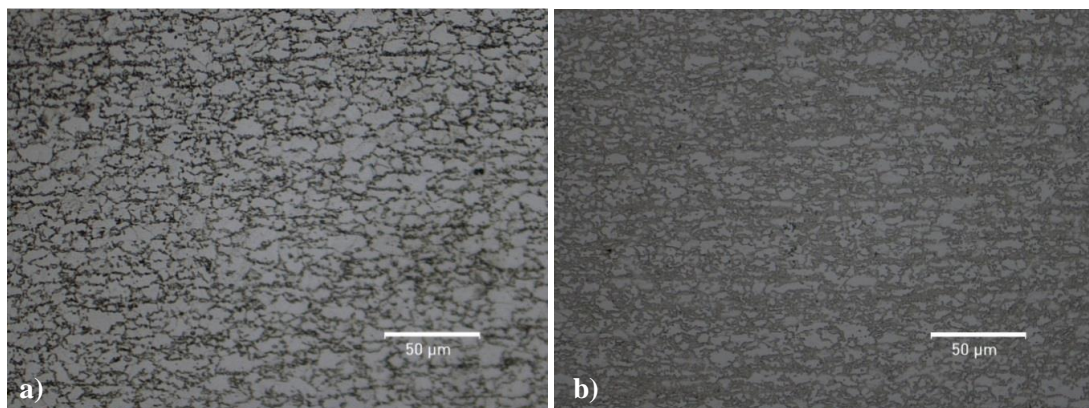


Figure 2.3 Microstructure images of a)DP590, b)DP800 as received condition

Dual-phase steels are useful only if they have a homogeneous microstructure. Therefore, it is important to have fine ferrite grains and a distributed martensite phase in the structure. DP steels can be produced by the controlled heat treatment process from the intercritical region (ferrite + austenite region) [21]. As known, ferrite is a stable phase, which means once it forms it cannot transform into any other phase (unless it is heated above the austenization temperature), thus, martensite phase is

formed from the austenite in the critical region. The amount of the martensite and ferrite for different grades of DP can be attained by changing the parameters such as heating rate, quenching medium, annealing temperature etc.

For instance, figure 2.4. [14] is explaining the DP steel production with the continuous annealing process from the ferrite – pearlite or ferrite – bainite steels. These steels are heated to the intercritical region or 100 % austenite region. Heating temperature is determined according to the C composition of the steels from the temperature&composition graph. If they are heated to the austenite-ferrite regions (above A_{c1}), all pearlite or bainite phase transforms into the austenite, then with quenching below to the martensite start temperature, austenite phase transform to the martensite. Moreover, if these steels heat to the 100 % austenite region (above A_{c3}), it is essential to arrange the cooling rate as it is necessary to cut the ferrite line to form ferrite phase. After ferrite phase forms, the remaining austenite phase transforms to the martensite below the martensite start temperature. In the end, both heat treatments result in the DP steels.

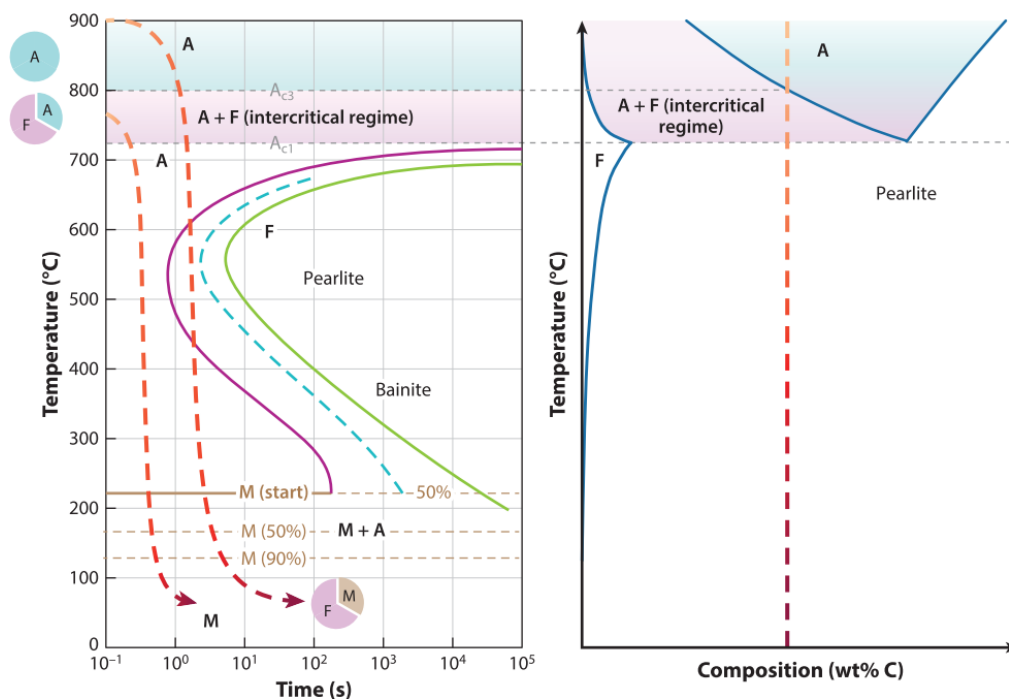


Figure 2.4 Heat treatment processes to observe Dual-Phase steels [14]

2.2. Mechanical Properties of DP Steels

DP steels are distinguished from conventional steels with their superior mechanical properties. Therefore, many studies have been performed in the literature to explain mechanical features of the DP steels [22]. Mechanical property of the material directly depends on the microstructure of the material. DP steels form two different phases; hard martensite islands randomly distributed to the soft ferrite phases. Although this approach similar to the basic composite definition, the rule of mixture cannot apply to determine their mechanical properties, due to the difference in strains and stresses of these phases. In this type of structure, soft phase, i.e. ferrite, is deformed more than the hard phase. Although, formability of martensite very small; it is capable of carrying the applied load; owing to martensite phase, DP steels can tolerate high-stress values.

Results of different studies in the literature confirm that the amount of martensite determines the strength of DP steels [23], [24], [25]. As martensite fraction of the DP steel increases, the tensile strength of the DP steel is also increases since martensite phase is able to carry most of the load that applied to the ferrite [23]. Note that the carbon content in steel is also an important parameter that determines martensite amount, which is related to the loading capacity [23].

Besides, the morphology of the martensite phase is also an important consideration that affects the strength of the steel. According to Molaei (2009) [26], DP steel that contains fibrous martensite displays higher strength compared to the network martensite structure DP steel. This difference arises from the distribution of the martensite in the ferrite matrix. Fibrous martensite has a better distribution in the matrix compared to the network structure martensite.

On the other hand, high amount of martensite causes a decrease in the ductility of the dual-phase steels. Martensite phase has low fracture toughness, and the ferrite phase has low strength. If one of the phases localizes, then the DP steels can exhibit an undesirable mechanical characteristic. Therefore, optimization of the mechanical

properties according to the desired application depends on the phase fractions, and it is a critical issue not to face any problems during their deformation [27].

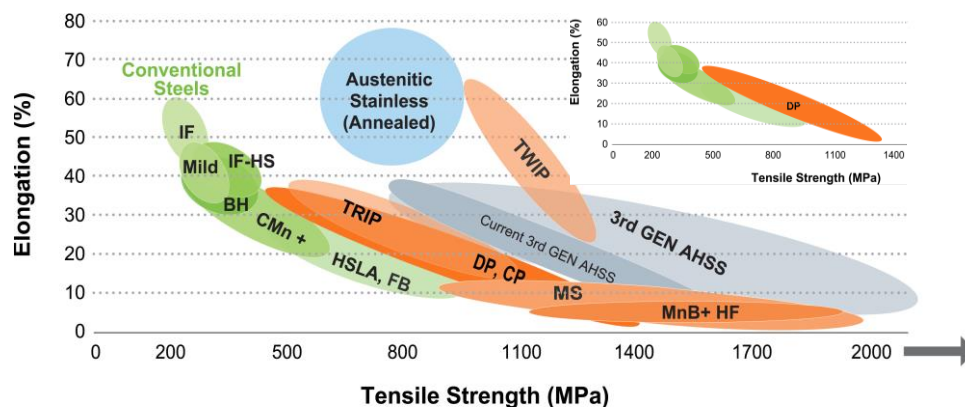


Figure 2.5 Comparison of the mechanical properties of Dual Phase Steels with others [28], [29]

Dual-phase steels exhibit higher elongation concerning some of the AHSSs (Fig. 2.5) [28], [29]. Higher elongation is an advantage for sheet metal forming; however, as seen from the figure 2.5 for some grades of DP steels, elongation is decreasing due to the increasing martensite amount in different grades. To eliminate this adverse effect of the martensite, different heat treatment procedures were reported in a study on DP steels [30].

Ductility of dual-phase steels is related to the ferrite phase amount. Some of the additive elements using in the production of DP steels are ferrite stabilizers. Therefore, the amount of these additives controls the ferrite fraction in the steel which directly affects the ductility. Moreover, strength of the ferrite could also increase using the alloying elements such as Mn, P and especially Si [22]. Adding Si causes high increase in the ductility; therefore to have optimum strength and ductility P is added due to its ductility decreasing effect [31]. In this way, strength and ductility balance in the DP steels can be maintained.

2.3. Forming of DP Steels

As mentioned earlier, DP steels are utilized for structural parts such as the chassis or car body structure in the automotive industry. Since DP steels have a complex microstructure, they deteriorated more compared to the conventional steels under industrial forming conditions. Therefore, combining high strain rate and high temperature can result in scrap parts or failure during forming. Since these sorts of problems may arise, it is essential to perform the forming process of structural parts precisely.

There are three different types of forming conditions depending on the operating temperatures. They are hot, warm, and cold forming. Hot forming is not a suitable option for shaping of the DP steels because of its two-phase structure. Under hot forming conditions, these steels can lose their superior mechanical properties. However, warm forming ($0.35T_{\text{melting}} < T < T_{\text{recrystallization}}$) operates at intermediate temperature conditions, which allows recovery of the material; but it is below the recrystallization temperature [32]. DP steels generally are shaped under the cold forming ($T < 0.35 T_{\text{melting}}$) conditions. However, because of the heating during deformation, some parts of the steel sheet can reach the warm forming temperatures. So, it can be said that DP steels deform under both cold and warm forming conditions.

DP steels have much more uniform elongation compared to the other types of steel which means it has much more formability due to the low yield strength/ultimate tensile strength (YS/UTS) ratio. In sheet metal forming applications, high impact energy absorption is another desired condition for formability. In figure 2.6, absorbed energy at a specific stress level graph of different types of steel is given. As seen from the graph, TRIP and DP steels, which are the prominent members of AHSS, have high energy absorption values at high stresses, compared to the others [33].

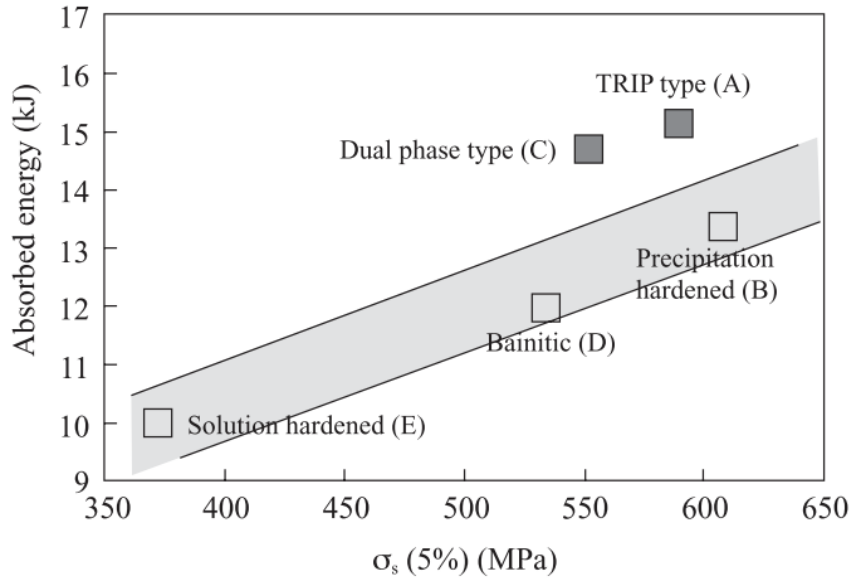


Figure 2.6 Absorbed energy vs. Stress graph of the different types of steels [33]

Besides temperature, strain rate sensitivity, strain hardening exponent, are other important parameters that affect the formability of DP steel. Generally, higher strain hardening exponent allows better formability in DP steels. Moreover, higher strain rate sensitivity means that although the strain rate changes it prevents the possible strain localization in a given area. Therefore, higher strain rate sensitivity is a better condition for the forming process.

On the other hand, in some deformation conditions, these parameters can change and have lower values as they both have a dependency to the deformation parameters. Thus, to have the desired property in a final product, all forming steps should be carefully applied and parameters needed to be controlled.

Because of its composites like structure and prominent properties, DP steels are challenging and therefore interesting research topics. For instance, Korzekwa et al., published a study that examines the deformation behavior of the DP steel in a microscale [34]. Based on TEM studies, they focused on the dislocation distribution differences between phases. According to the interpreted results, dislocation density

is high near the martensite ferrite interface meanwhile observed dislocation density inside the ferrite grains is low.

Also, in figure 2.7 [34], Jaoul-Crussard analyse graph of typical DP steel given with the strain hardening stages. This graph shows different level of strains. At those strain values points mark on the graph. At those points TEM studies were performed to get more information.

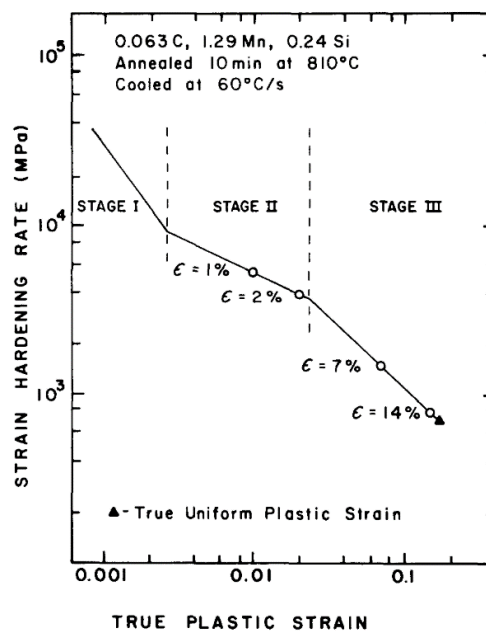


Figure 2.7 Jaoul-Crussard analysis graph of typical DP steel is given with the strain hardening stages [34]

At the beginning of the deformation, while $\epsilon = 1\% - 2\%$, planar dislocation walls and already formed dislocation cells are observed near to the martensite phase. In addition, while $\epsilon = 7\%$, the dislocation cell structure with thicker cell walls was obtained that locates near to the martensite islands with smaller cell size. Furthermore, while $\epsilon = 14\%$, nevertheless, the cell walls got thinner, such thinning was not cause a further

reduction in the cell size (fig 2.8) [34]. As seen from this study, ferrite phase can be examined easily; however, the very high initial dislocation density of the martensite limits the investigation of the steps of plasticity in TEM scale.

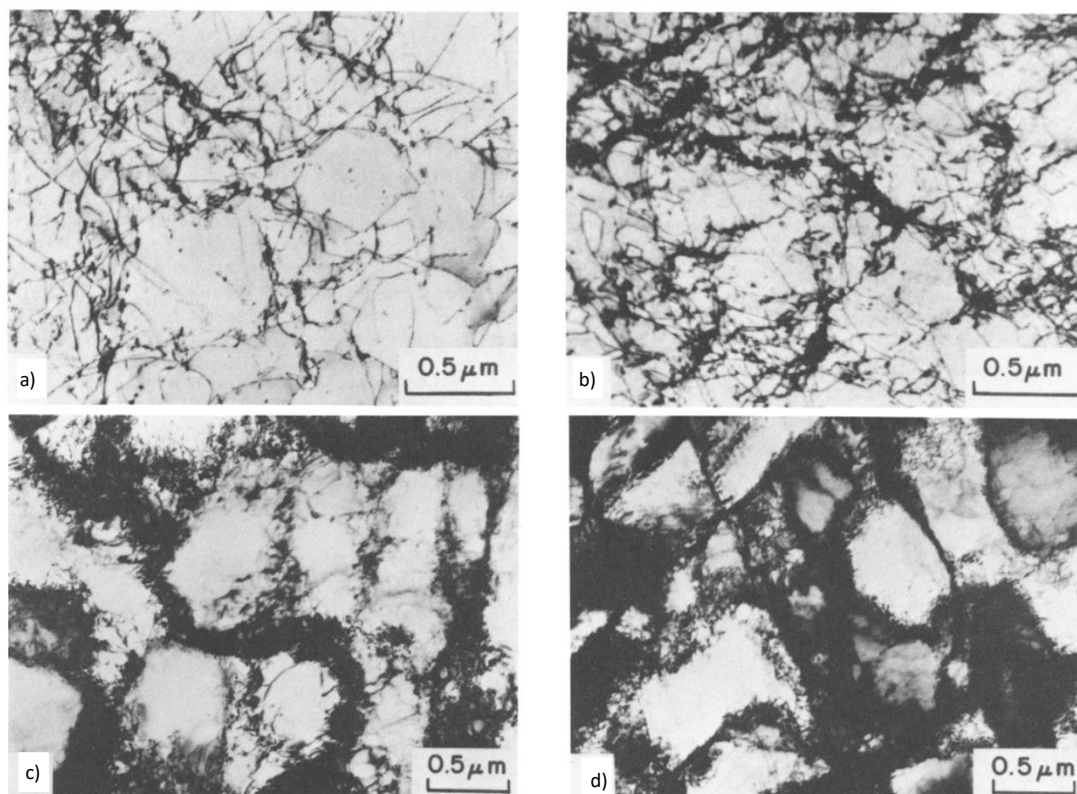


Figure 2.8 TEM images of the DP steel at different stages and strain values; a)1% strain, dislocation tangles, b)2% strain, already formed dislocation cell structure, c)7% strain, dislocation cells in ferrite, d)14% strain, dislocation cells in ferrite [34]

2.4. Dynamic Strain Aging in DP Steels

Static strain aging mechanism in other words a yield point hardening, is needed to explain before starting any further explanation. During a tensile test, when applied stress value higher than the yield stress the material goes into the plastic deformation region. And then if applied load removed, carbon solute atoms (Cottrell) diffused through around the dislocations and located there [35]. This will harden the material

and so that when the load applied to a material a new yield point will be higher than before. This is called a yield point hardening. In this way, the material has a new higher yield point but the ductility of it will be decreased.

Strain rate and temperature are the major factors that create aging conditions. For instance, at high strain rates, dislocations move faster so carbon atoms cannot catch the dislocation. Therefore, no aging occurs. On the other hand, at the low strain rate experiments, movement of the solute atoms faster compare to the dislocations so they are not meet and no aging occurs, again. Likewise, at high temperatures, the diffusion rate of the carbon atoms will be high with respect to the dislocation motion thus, no aging happens. When low-temperature tests consider, the diffusion rate of the solute atoms may be lower than the dislocation motion, as a result, aging phenomenon may not be observed. To conclude, dynamic strain aging is a mechanism which appears during the tensile tests at the specific strain rate, temperature and strain values depending on the test parameters [36], [37], [38].

During deformation, temperature and strain rate meet at some point so the DSA mechanism may appear especially at the high strain rates and adiabatic heating conditions [39], [40]. Oppose to the static strain aging, locking and unlocking of dislocation solute atom relation occurs in row after row and followed by stress relief, which results in unstable flow behavior. Therefore, in industry, forming at the conditions which DSA may happen limits the formability of the material.

Serrations in the stress-strain curves are the main symptoms of the DSA mechanism. These serrations are observed by Le Chatelier and Portevin while working with mils steels and aluminum alloys respectively. Therefore, this type of unstable flow named a PLC effect [41]. DSA behavior was observed in many types of steel in literature [42]–[44].

When solute carbon atoms catch the dislocation, it acts as a drag force and decreases the rate of the dislocation [45]. If a dislocation is able to get over the solute atom, it continues to its motion until it encounters with another solute atom. This repeatable

process shows itself as serrations in the stress-strain curves. In that case, although the strength of the steel increased, ductility will be decreased [26].

DSA is an undesirable mechanism during the deformation of the steel sheets. Therefore, many precautions tried to apply such as using additives, changing carbon content and many others. However, all these are not permanent methods to avoid DSA. The most reliable solution of this undesirable mechanism is, managing the parameters so the material never gets into the DSA range during deformation.

In addition to the serrations in the stress-strain curves, there are other signs that shows the DSA mechanism activity in the deformation [46], negative strain rate sensitivity is one of them [8], [38], [46]. If a material exhibits unstable plastic flow during deformation, it means strain rate sensitivity of the material is negative.

Bayramin et al. [8], [38] studied dynamic strain aging behavior of the DP steels in forming applications. In that study, two different grades of DP steel tensile tested at different strain rates and temperatures. As understood from the figures, DSA is active at 200-300 °C temperatures and relatively high strain rate (Fig. 2.9-10), meanwhile at RT, 100 °C and 400 °C, DP steels showing expected deformation behavior. Furthermore, due to the high amount of ferrite in DP590, DSA mechanism is more effective compared to the DP800. Strain rate sensitivity values of the samples are also calculated and it is observed that at the DSA range strain rate sensitivity has a negative value for both grades. Therefore, it is concluded that during warm forming conditions DP steels can enter DSA range, which is an undesirable condition especially for the massive production in the industry.

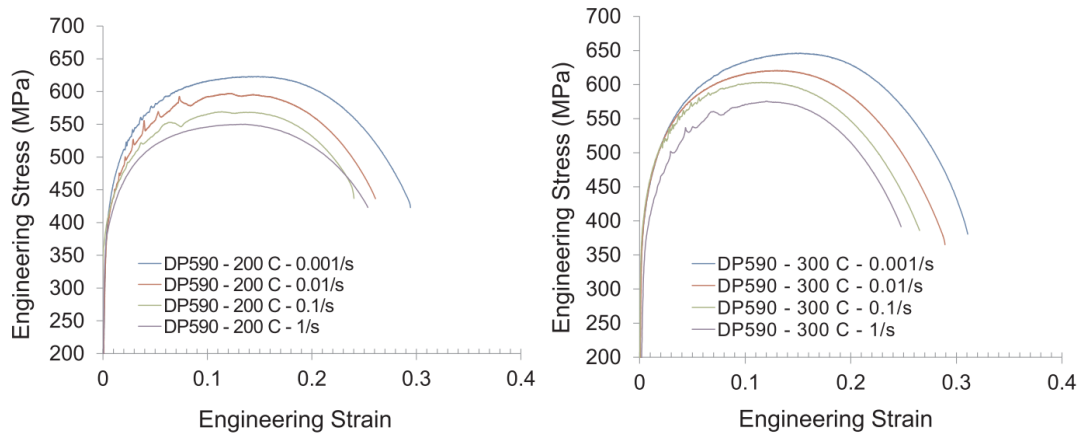


Figure 2.9 Stress strain graph of DP590 observed after tensile tests at different strain rates and temperature (DSA range) [8]

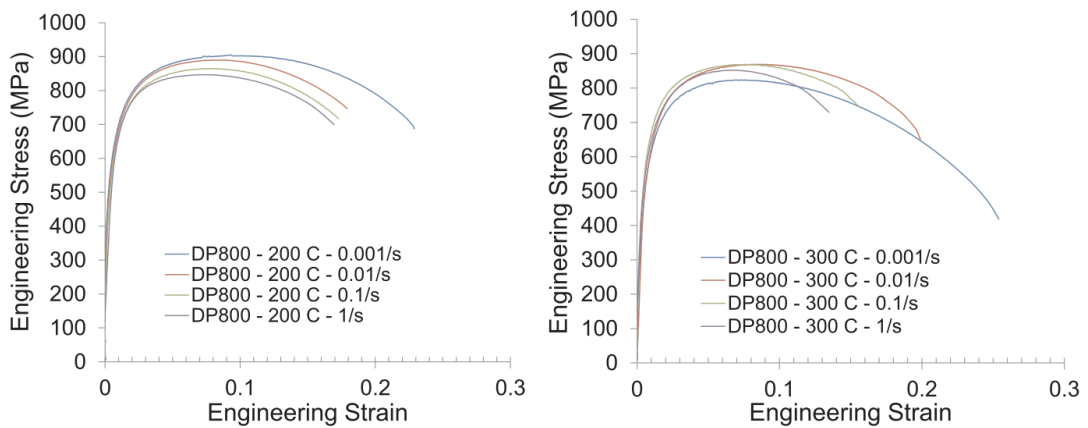


Figure 2.10 Stress strain graph of DP800 observed after tensile tests at different strain rates and temperature (DSA range) [8]

2.5. Damage in DP Steels

DP steels consist of two different phases, due to the strain mismatch between martensite and ferrite phases, microcrack formation is easier. Yet, these microcracks could be omitted by localized deformation and hardening in ferrite, therefore, DP

steels do not follow the brittle type of fracture [14]. Damage is strongly dependent on the microstructural properties such as martensite amount or martensite-ferrite interface. Since damage is an interesting research topic many studies have performed to understand the damage behavior in DP steels. For instance, Stevenson [47] and Mazinani&Poole [48] stated that, damage nucleation is obtained primarily in the martensite zones. Moreover, Avramovic-Cingara et al [49] studied the DP600 grade and interpreted that most of the failures occur due to the mismatch between martensite and ferrite phases. They also concluded that if martensite has banded morphology, then damage mostly observed in martensite [50].

As explained, it is essential to understand the damage and to observe the damage value inside the steel before it fails if it is possible. The most common method of monitoring damage evolution is to evaluate the volume ratio of voids inside the material after deformation [17]. To detect the porosities formed in material, scanning electron microscope (SEM) characterization is needed under different strain conditions [51], [52]. X-ray microtomography is another technique used to determine porosity amount. Even though the resolution of this technique is limited compared to the SEM, it is very useful for a macro-scale analysis [16], [53], [54]. In addition to microstructural analysis, changes in physical properties like volume, density can be used for damage parameter calculations. However, they are rougher than the micro-scale analyses [55].

Damage parameter can also be obtained by mechanical property-based techniques. One of these techniques is to calculate the change in the elastic modulus [17]. Elastic modulus measurements are commonly performed with the extensometers during uniaxial tensile testing. Extensometers are able to measure the strain value accurately during the plastic deformation, however they are not that accurate in the elastic region [56]. The elastic modulus values calculated by the extensometer and resonance frequency and damping analysis (RFDA) methods can show significant discrepancies, despite the same sample size [57]. A good comparison of determination of damage parameter using different techniques can be found in literature [58].

All these challenging facts in calculating the damage parameter led researchers to study simulation and modeling rather than experimental studies. Although modeling and simulations have provided many advantages to researchers to evaluate damage parameters, they usually were not supported by experiments. Also, these studies mainly focused on DP600 and TRIP steels [59], [60] and the ones that compare two different dual-phase steel have been operated at low strain rate ($3 \times 10^{-4} \text{ s}^{-1}$) [61]. Studies involving only experiments were also done at lower strain rates compared to the industrial strain rates [6], [7], [12].

2.6. Main Findings and Gaps in Literature

DSA is a threat to forming of DP steels since it can cause flow instabilities during deformation. DSA phenomenon may appear in DP steels under different industrial forming conditions, which resulting in abnormal damage formation. Therefore, a systematical study on thermomechanical forming conditions is necessary to understand the damage and DSA relation.

Any experimental study about damage at high strain rate and high temperature does not exist in the literature as reviewed. Most of the studies related to damage, based on modeling and experiment-based studies were not done at industrial forming conditions. So that, damage on the DSA range of the DP steels was not investigated, and DSA- damage relation was not explained in the literature. In addition, DSA in DP steels may have different responses based on the phase amounts of ferrite and martensite. Damage behavior of different grades is not fully explained in the literature as an experimental study.

In this thesis, it is aimed to investigate the damage behavior and observe damage parameters of DP steels under industrial forming conditions. To do that, a set of thermomechanical conditions was determined, and the results of mechanical tests were analyzed and compared with micro characterization studies.

CHAPTER 3

MATERIALS AND METHODS

3.1. Materials

DP590 and DP800 grades of steel, which are the most used ones in the automotive industry, were used in this study. The chemical compositions of these steels, obtained from Swedish Steel Works (SSAB), are given in table 3.1. Their main difference arises from the carbon amount.

Table 3.1 Chemical compositions of DP590 and DP800

Mass Contents (%)	C	Si	Mn	P	S	Cr	Mo	Ni	Cu	Al	Fe
DP590	0.081	0.284	1.517	0.008	0.004	0.02	0.006	0.033	0.015	0.038	97.90
DP800	0.12	0.194	1.549	0.007	0.002	0.035	0.009	0.025	0.011	0.032	97.89

3.2. Digital Image Correlation (DIC) Tests

DIC tests were operated at the TA-BAEHR DIL805A / D-Deformation Dilatometer (Fig. 3.1.) which is in Metal Forming Center of Excellence in Atılım University.



Figure 3.1 TA-BAEHR DIL805A/D-Deformation Dilatomete

3.2.1. Digital Image Correlation (DIC) Technique and Sample Preparation

DIC is a technique in which data received by the optical camera is processed. The movement of particles with different gray contrast is monitored by sequential images with which the contrast information generated by the particles in the digital image pixels is correlated. The displacement of particles from these digital images recorded with the help of the camera is analyzed with the help of computer software and the analysis gives information on the strain of the material. Strain maps indicate the location of the flow and where the strain is concentrated locally. Therefore, DIC is a method that can be used to study the flow behavior of steels.

The measuring areas of the samples (parts examined by the optical camera) were prepared by using metallographic methods (grinding, polishing). A solution of 70% acetone and 30% acrylic black matt paint was sprayed on this polished surface with a Bad Sector BD-130 airbrush operating at a pressure of 45 psi from a distance of about 10 cm. This method created 20 μm black dots on the surface, and a pattern suitable for digital image correlation was obtained. Besides, the metallographic polishing process prior to spraying created a white area on the background of the pattern, creating a suitable contrast for DIC.

3.2.2. Digital Image Correlation (DIC) Tensile Tests and Experimental Setup

2 mm DP590 and DP800 steel sheets were cut parallel to the rolling direction by electrical discharge machining (EDM) according to the dimensions given in figure 3.2. because the cutting process requires precision. The test matrix determined for DIC experiments is provided in the table 3.2. These tensile tests continued until the samples ruptured.

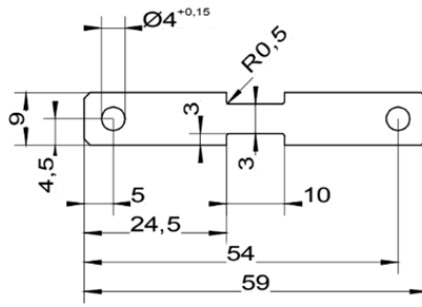


Figure 3.2 Technical drawing of the DIC testing specimen using in TA-BAEHR DIL805A/D-Deformation Dilatometer. Dimensions are in millimeter.

Table 3.2 Experimental matrix of DIC tensile tests

<i>Grades</i>	DP590				DP800			
<i>Strain Rates</i> (s^{-1})	10^{-3}		1		10^{-3}		1	
<i>Temperatures</i> ($^{\circ}C$)	RT	200	RT	200	RT	200	RT	200

After the room temperature tests were completed, the horizontal induction coil was used in dilatometer for high-temperature tests (Fig. 3.3(a)). Thermocouples are welded to the samples for temperature control in high-temperature tests. The thermocouples used are compatible with the device and differ from the conventional thermocouple (Fig. 3.3 (b)). The thermocouple welding process was carried out with a particular device capable of spot welding (Fig. 3.4). The sample to which thermocouple was welded and ready to be test is given in the figure below (Fig. 3.5).

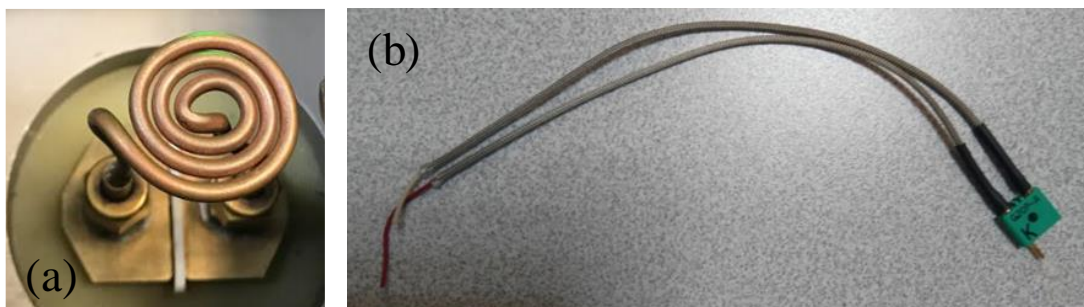


Figure 3.3 a) TA-BAEHR DIL805A/D horizontal induction coil; b) K type thermocouple i.e. suitable for dilatometer



Figure 3.4 Spot welding device for thermocouple welding to sample for temperature control of dilatometer

For high-temperature experiments, heating was carried out on the induction coil on the dilatometer. Throughout the experiment temperature was monitored via thermocouple, heating rate was constant and determined as $10^{\circ}\text{C} / \text{s}$. At the end of the experiments, cooling rates was determined as $25^{\circ}\text{C} / \text{s}$.

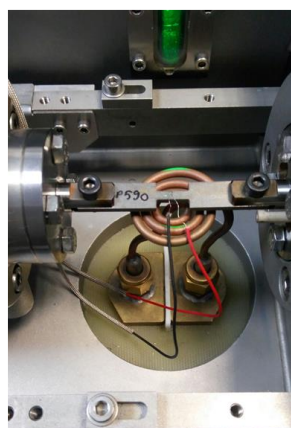


Figure 3.5 Thermocouple welded sample placed in dilatometer

Basler acA2000-165uc- ace model camera was used for optical image recording. This camera is equipped with a continuous magnifying lens i.e. Navitar UltraZoom 6000 brand and model, and the Navitar coaxial light source. This camera equipment was fixed to the TA-BAEHR DIL 805A / D deformation dilatometer with the help of a tripod in a position to view the measuring area of the sample vertically (Fig. 3.6). 1.4X magnification was used for the experiments and the field of view was $7.9 \times 4.2 \text{ mm}^2$. For experiments at a strain rate of 0.001 s^{-1} , the camera was set to receive 1 image per second (1 fps), and 140 images per second (140 fps) for 1 s^{-1} .

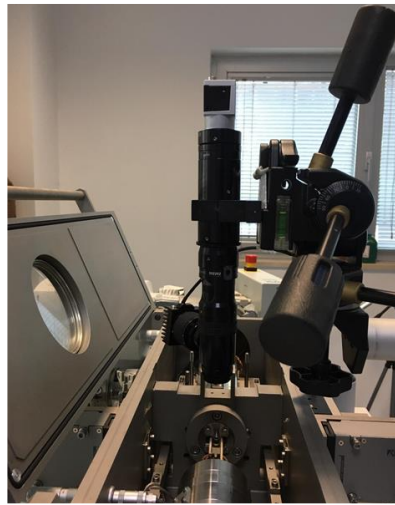


Figure 3.6 Experimental setup (Camera assembly with a tripod placed perpendicular to the sample)

3.2.3. Digital Image Correlation (DIC) Program and Strain Maps

Ncorr v1.2, a Matlab-based program, was used for DIC. The program performs a 2-dimensional digital image correlation and gives Lagrangian or Euler strain values in the x and y directions. Some of the photographs were taken for experiments at a strain rate of 0.001 s^{-1} were selected and loaded into the program for analysis. All photographs taken for experiments at 1 s^{-1} strain rate were uploaded to the program. 80 pixels for subset size and 10 pixels for step size were used for the DIC analysis. In general, the resolution was set to 0.0012 mm/pixel . The error in the strain value was

measured as 0.14%. In this case, the positional strain measurement resolution on the macro scale was 96 μm .

3.3. Microstructural Analysis

The microstructural analysis was required to get further information about experiments. Especially for the damage analysis, it was a must to examine the samples and detect the void percentages to discuss the relationship between change in the elastic modulus and damage. Moreover, the DIC experiments continued until the samples were fractured. Therefore, it was also important to examine the fracture surface and discuss their fracture behaviors. Both of these studies were done with the help of SEM.

3.3.1. Scanning Electron Microscope (SEM) Images

In this study, SEM was used for void analysis which is necessary for the damage, and fracture surface analysis of the samples used in DIC tests. So, this topic is divided into two items.

1. SEM for damage

Samples were cut from the middle of the gage with a precision cutter (Buehler, Isomet 5000). Then, they were prepared by classical metallographic methods (grinding, polishing and etching). The cross-sections of the samples were imaged by FEI Nova NanoSem 430 model SEM, operating at 18 kV. Void volume fraction analyses were done without etching and at least 21 images with 4800 μm^2 field-of-view were taken at each condition. These images were analyzed using ImageJ software by threshold void analyzed tool. After the void fraction analyses were done the samples were etched using nital (2% nitric acid, 98% ethanol) solution. Etched samples were used to visualize the shape and size of voids and their location with respect to the ferrite and martensite phases.

II. SEM for fractography

After the samples were fractured, parts were taken from the dilatometer carefully without touching the fracture surface. Then these samples were cut using the precision cutting device and surfaces were cleaned using the Ultrasonic cleaning device. Finally, their images were obtained using SEM.

3.4. Damage Analysis

Damage analysis was the primary concern of this study, explaining its mechanism and observing changes with respect to changing parameters, and DSA relation was therefore essential. In this section, all the methods using damage analysis were explained step by step.

3.4.1. Tensile Tests for Damage

2 mm thick sheets of DP590 and DP800 grades obtained from Swedish Steel Works, SSAB were used for this study. Firstly, the steel sheets were cut parallel to the rolling direction by EDM according to the dimensions given in Figure 3.7.

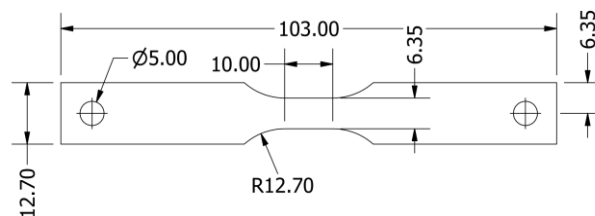


Figure 3.7 Technical drawing of the testing specimen

A series of tensile tests up to different strain levels was performed on a plastometer Gleeble® 3500, (Dynamic Systems Inc.) (Fig. 3.8) which is in Metal Forming Center of Excellence, Atılım University. The mechanical system of the plastometer is capable of performing various mechanical tests owing to its integrated closed-loop control system. The system can apply 10 tons of force both in compression and tension and the stroke rate is adjustable in between 1 $\mu\text{m/s}$ to 1000 mm/sec. All mechanical tests have repeatability and precise execution owing to Linear Variable Differential

Transformers (LVDTs) system and also contact-type extensometers [62]. This system was selected because of precise strain/strain rate control and high temperature capability.



Figure 3.8 Gleeble 3500 device

After a K-type thermocouple was welded to the sample to control temperature during the test, it was located chamber of the Gleeble (Fig. 3.9). The heating was performed by direct conduction and the temperature was controlled using the closed-loop thermal control. For high-temperature tensile tests, samples were heated at 10 °C/s up to the desired temperature and soaked for 60 seconds to obtain a homogeneous temperature distribution. The test was conducted with a homogeneous temperature distribution with a temperature difference of 10 °C between the gage and ends of the sample.



Figure 3.9 Tensile test sample located in the Gleeble the chamber before test

For the low strain rate (10^{-3} s^{-1}) experiments, a contact-type extensometer was used for precise strain measurements. The strain control was achieved with the extensometer and the stroke rate was adjusted accordingly to keep the strain rate constant during the experiment. Therefore, the measured strain results during the experiments were precise for the lower strain rates. On the other hand, standard contact extensometers could not be used at high strain rates ($\dot{\epsilon} > 2 \text{ s}^{-1}$) because of the low data acquisition rate. For the high strain rate (10 s^{-1}) experiments, stroke transducer was used for strain control. A calibration between the stroke and the strain was needed due to the machine compliance. For this purpose, tensile tests were performed at 1 s^{-1} with and without extensometer, and the correlation between stroke and strain was determined.

Overall, two different strain rates i.e. low strain rate and high strain rate (10^{-3} s^{-1} and 10 s^{-1}), three different temperatures (RT, 200 °C, 300 °C) and five different strain values were tested for both grades. For each condition, at least three experiments were carried out to have statistical significance. Experiment matrix of damage tensile test given in the Table 3.3. as a summary.

Table 3.3 Experiment matrix of tensile tests for damage analysis

<i>Grades</i>	DP590						DP800					
<i>Strain Rates</i> (s^{-1})	10^{-3}			10			10^{-3}			10		
<i>Temperatures</i> (°C)	RT	200	300	RT	200	300	RT	200	300	RT	200	300
<i>Targeted Strain</i> (%)	1, 2, 8, 16			1, 2, 8, 16			1, 2, 6, 10			1, 2, 6, 10		

3.4.2. Strain Measurements

Since the contact-type extensometers were not used at the high strain rates due to the low acquisition rate, target strain was applied with the stroke control. When the deformation was applied with the stroke, the applied deformation includes the compliance of the machine, the gap between the pins and pin holes of the specimen and also the deformation amount that is outside of the gage area. To validate the actual strain amount in the gage area, an optical metrology system (ARGUS, GOM Gmbh.) was used which is in the Metal Forming Center of Excellence in Atılım University. The system is specially designed to be used in sheet metal forming applications. It ensures reliable results in both small and large components since it has high local resolution and all measurements are independent of the material [63].

During the strain measurements, a certain speckle pattern was applied to the surface of samples before the tensile tests. The shape and dimensions of the speckles in the original pattern change after the deformation, and a camera records the initial and final patterns. Using the change in patterns, strain values were determined with the help of the Argus software (Fig. 3.10).

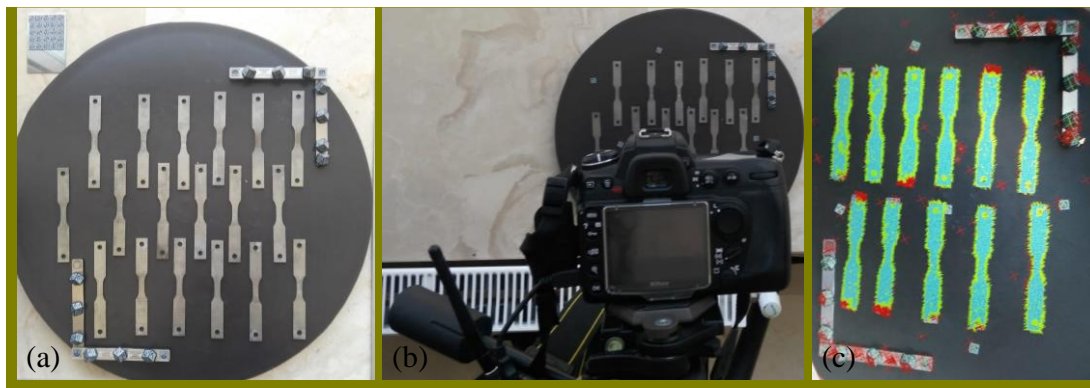


Figure 3.10 Samples a)after tested preparing for the Argus analysis, located with the help of Argus apparatus; b) photos were taken for the analysis; c) Argus analysis started based on the taken photos.

Three examples from the Argus measurements result are shown in Figure 3.11. They belong to the DP590 steel samples tested at 10 s^{-1} strain rate and $300 \text{ }^\circ\text{C}$. Scale bar, next to the samples, shows the measured strain values after the experiments. The measured strains are homogenous at the gage region, where the maximum difference between the actual and target strains is $\pm 1.5\%$. So, suggested calibration strategy is validated. Targeted and actual strain values for all the experiments are given in Table 3.4 together with the experimental matrix.

Table 3.4 Experimental matrix with the targeted and measured strain values

<i>Grades</i>	DP590						DP800					
<i>Strain Rates</i> (s^{-1})	10^{-3}			10			10^{-3}			10		
<i>Temperatures</i> ($^\circ\text{C}$)	RT	200	300	RT	200	300	RT	200	300	RT	200	300
<i>Targeted Strain (%)</i>	1, 2, 8, 16			1, 2, 8, 16			1, 2, 6, 10			1, 2, 6, 10		
<i>Measured Strain (%)</i>	1, 2, 8, 16			1, 1.5, 7, 16			1, 2, 6, 10			1, 3, 7.5, 11		

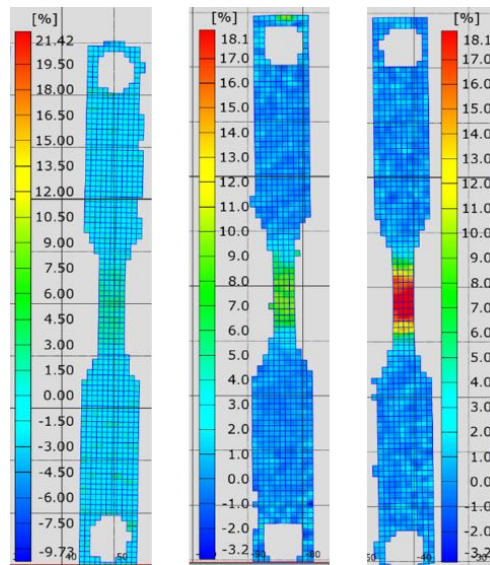


Figure 3.11 Argus analysis results of three different samples (DP590, 10 s-1 strain rate, 300 °C) tested at target strain values of 2%, 8%, 16% (from left to right).

3.4.3. Elastic Modulus and Damage Parameter Measurement

According to the Lord and Morrell [56], the best way to measure elastic modulus is the resonant frequency damping analysis. However, dimensions of the sample restricted to use of RFDA device in this work. Therefore, the ultrasonic sound velocity measurement (USVM) technique was used instead. USVM was also faster and practical than RFDA.

The sound velocity measurement technique is generally used for non-destructive tests (NDT). Sound waves are sent through the samples using both perpendicular and transverse probes, and then the time that passes during the wave travel between measurement points is recorded. Panametrics, 5MHz probes were used in Olympus-Epoch50 device. Before doing the measurements, it is important to use lubricant like oil or honey to transfer the waves directly to the samples. As explained by Panakkal [64], the elastic modulus (E) can be calculated using :

$$E = \frac{\rho V_t^2 (3V_l^2 - 4V_t^2)}{(V_l^2 - V_t^2)} \quad (1)$$

where ρ (kg/m^3) is the density, V_l (m/s) is longitudinal ultrasonic velocity and V_t is transverse (or shear) ultrasonic velocity. Damage parameters of the tested samples were calculated from the measured elastic modulus values by using:

$$D = 1 - \frac{E_f}{E_0} \quad (2)$$

where E_0 and E_f is the elastic moduli of initial and tested conditions, respectively [17].

In order to test the reliability of the USVM, elastic modulus of the as-received sheets were measured with both methods and compared with each other. For instance, elastic modulus of the as-received DP800 sample was 209.37 GPa with RFDA meanwhile it was 210.11 GPa with USVM (0.35% difference). Damage parameters from both methods were also compared with each other for the DP800 samples deformed at 10^{-3} s^{-1} , room temperature and 300 °C. In this case, the sample size was larger to obtain reliable measurements from RFDA.

As seen from Table 3.5, the damage parameter results are close to each other at each strain level. On average, the values deviate from each other by 27%, and the deviation decreases at higher strains. The minimum deviation of 5% (0.037 vs 0.039) occurs at 6% strain, 10^{-3} s^{-1} strain rate, and 300 °C, while the maximum deviation is 70% at 2% strain, 10^{-3} s^{-1} strain rate, and 300 °C. Overall, these results confirm the reliability of the USVM for damage parameter measurements. Moreover, for damage analysis, the change in damage parameters is more critical than the absolute damage values and the usage of single technique ensures consistent measurements of damage.

Table 3.5 Comparison of RFDA and USVM damage measurements for deformed DP800 samples

DP800	<i>Strain (%)</i>	<i>1</i>	<i>2</i>	<i>6</i>	<i>10</i>
<i>10⁻³ s⁻¹, RT</i>	RFDA	0.008	0.012	0.039	0.039
	USVM	0.005	0.016	0.028	0.031
<i>10⁻³ s⁻¹, 300 °C</i>	RFDA	----	0.007	0.037	0.057
	USVM	----	0.024	0.039	0.053

CHAPTER 4

RESULT AND DISCUSSION

4.1. Macro DIC analysis of DP steels

4.1.1. DIC Results of DP590

DIC analysis results are given with the help of photographs taken while the DP590 steel is tensile tested at given strain rate and temperature. These images were taken from the measurement region of the samples, and the scanned area is approximately 12 mm². Images of DIC analysis (Fig. 4.1-4), and strain stress curves (Fig. 4.5) are given below. The given stress-strain graphs belong to DIC tested samples.

To compare the samples, the photographs were selected at the same strain values. The scale bars represent the strain amount accumulate in the samples. For some samples more photographs were selected since the DSA phenomenon is an important issue at those parameters.

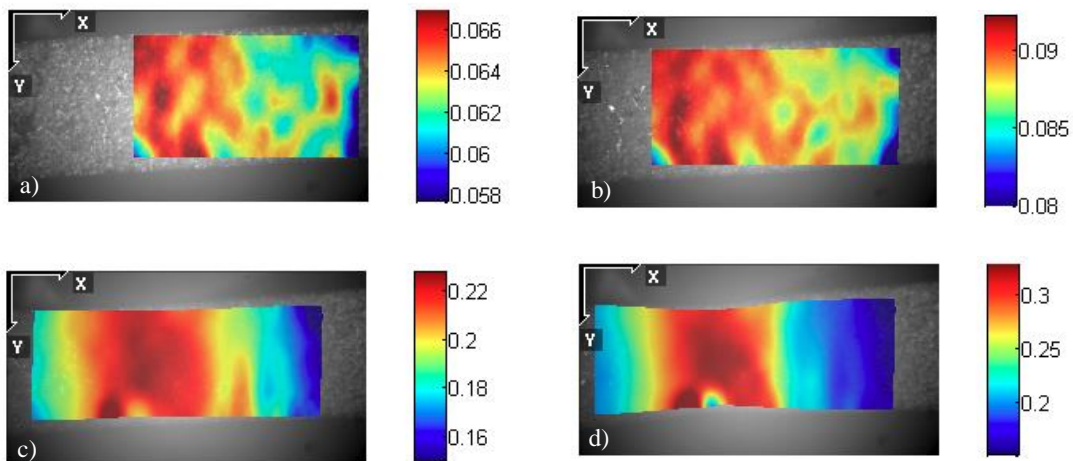


Figure 4.1 DP590 RT 10^{-3} s^{-1} ; a)5%, b)10%, c)20% [before neck], d)23% neck strain, DIC analysis

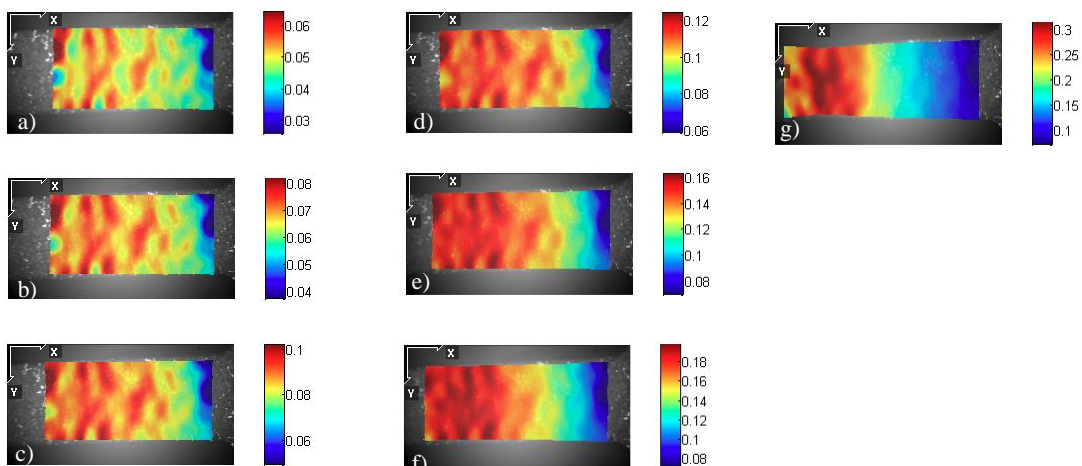


Figure 4.2 DP590 RT s^{-1} ; a)5%, b)6.7%, c)8.65%, d)10.7%, e)14.1%, f)16.4%, g)18.8% (neck) strain, DIC analysis

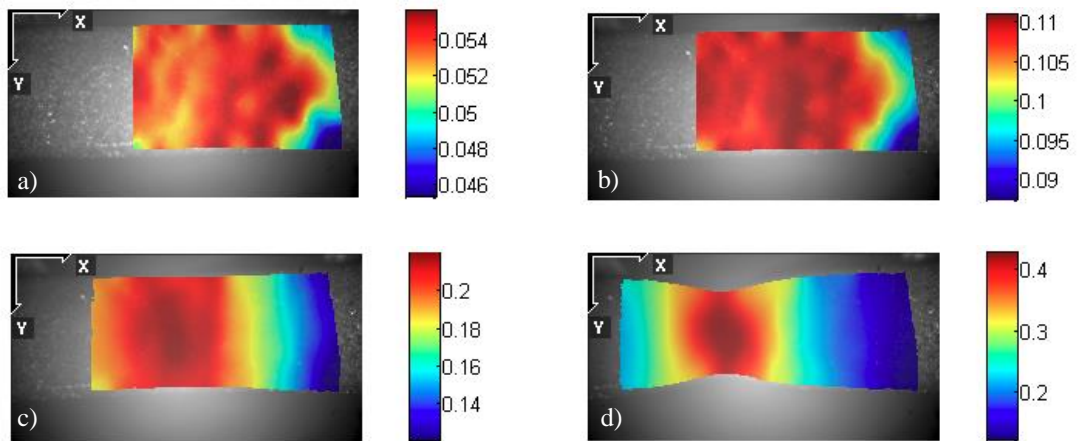


Figure 4.3 DP590 200°C 10^{-3} s^{-1} ; a)5%, b)10%, c)20% [before neck], d)24% neck strain, DIC analysis

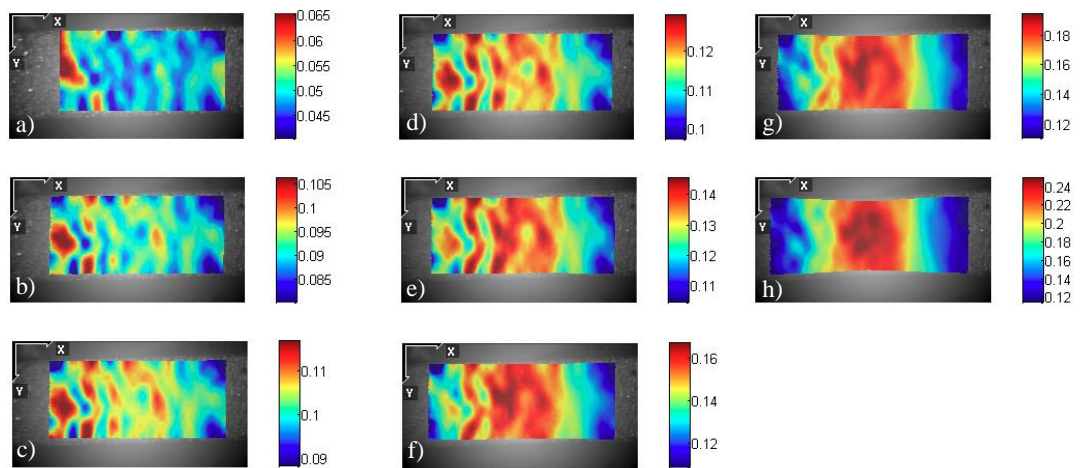


Figure 4.4 DP590 200 °C s^{-1} ; a)5%, b)9.1%, c)10.4%, d)11.6%, e)13.02%, f)14.5%, g)16%, h)18.3%(neck) strain, DIC analysis

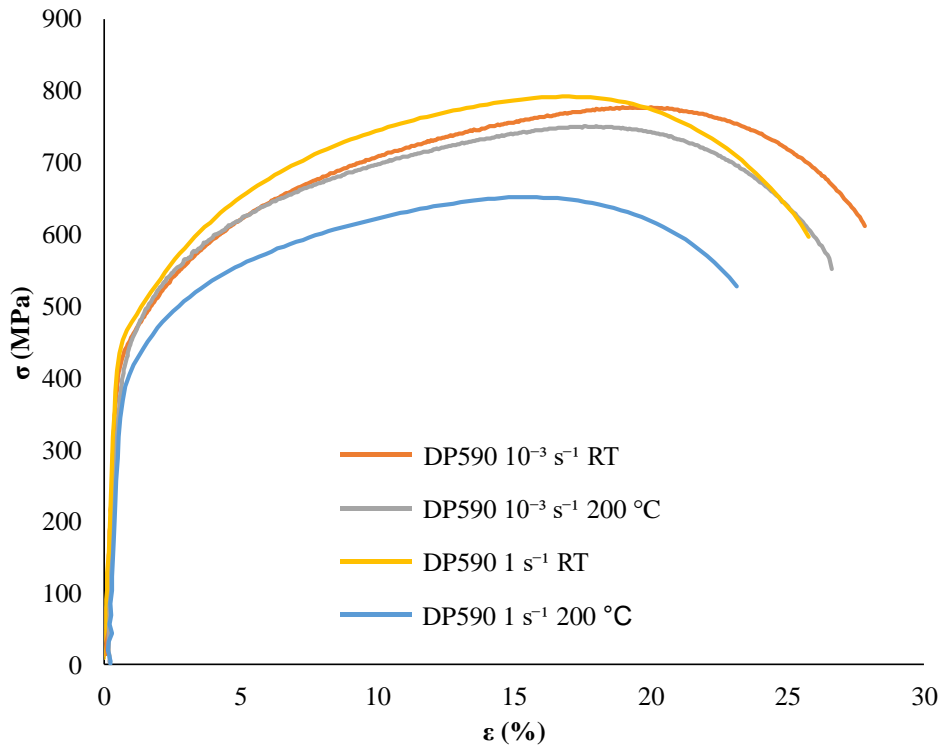


Figure 4.5 Stress&Strain curves of the DIC analyzed DP590 samples observed from tensile tests

When DIC images obtained from Figures 4.1 and 4.2 are compared, the effect of strain rate on room temperature can be seen. Strain serrations observed at high strain rates are not present at low strain rates. However, localization is also seen, and this can be attributed to the fact that the material has two different phase structures. In this case, it is understood that there is localization especially in certain regions in the distribution of strain.

Also, when compared to figure 4.3 and figure 4.4, it is seen that high temperature along with the strain rate causes this condition and increases its effect. It can be concluded that the high strain rate affects the flow instabilities and the DSA mechanism more than the temperature.

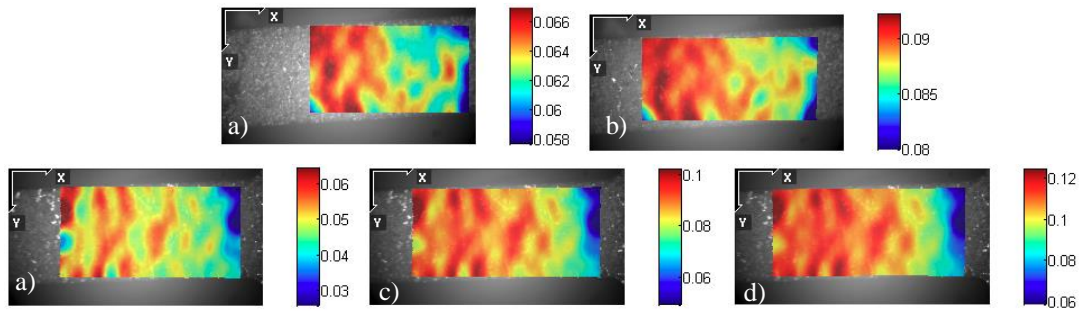


Figure 4.6 DP590 RT 10^{-3} s^{-1} ; a) 5%, b) 10%; DP590 RT 1 s^{-1} ; a) 5%, c) 10%, d) 11% strain DIC analysis

Figure 4.6 shows DIC images taken for the same strain values at room temperature but at different strain rates. When looked at, there is a more homogeneous strain propagation at the low strain rate, but when the strain rate is increased, it turns into a banding-like structure. This banding-like structure started at a low strain (5%) and became more visible as the strain increased and accumulate, after which the band structure caused a neck at some point.

Strain localization is more prominent for the high strain value, so it can be said that the deformation is happening as the strain accumulated in these structures. This behavior is more homogeneous at low strain rates. This result shows the effect of the strain rate by DIC method.

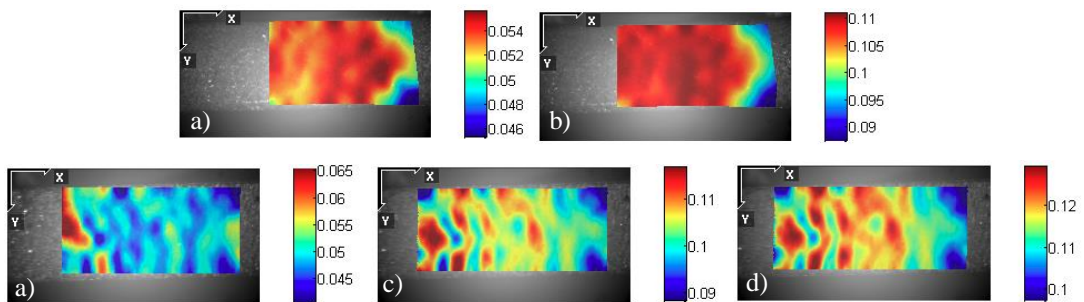


Figure 4.7 DP590 $200 \text{ }^{\circ}\text{C}$ 10^{-3} s^{-1} ; a) 5%, b) 10%; DP590 $200 \text{ }^{\circ}\text{C}$ 1 s^{-1} ; a) 5%, c) 10%, d) 11% strain, DIC analysis

In Figure 4.7, there are images taken from DIC analysis of the DP590 steel at the same strain values at 200 °C, different strain rates. When we compare low strain rate and high strain rate for 5% strain value, a homogeneity is observed at low strain rate, while fluctuations in strain observed at the high strain rate. It is seen that these waves become more apparent with the increasing amount of strain, and the strain is accumulating on them. At low strain rate, it was found that the deformation continued homogeneously until the sample reached the necking strain, while at the increased strain rate it progressed in the form of banding. This situation is clearly seen in the DIC analysis of both room temperature and 200 ° C experiments. It also appears that this situation becomes visible with increasing temperature when comparing room temperature and 200 ° C experiments at high strain rate. However, at low strain rate, there is no such difference when room temperature and 200 °C are compared.

When we look at the results obtained in the damage parts, dynamic strain aging (DSA) mechanism is observed in both DP590 and DP800 steels, and this situation is more dominant for the DP590 steel. One of the clear indicators of DSA behavior on a macro scale, although not always, is the formation of Portevin Le-Chatelier (PLC) bands. Serrations in the stress-strain graphs are considered as an indicator of PLC bands, but they are not the only indicators for DSA. Although these serrations not observed in every experiment, they are seen in some experiments which identified as the DSA interval. These results can be associated with band-like images obtained from DIC studies in the literature [65]. As mentioned previously, DSA conditions may occur during production in the industry and it is possible to see PLC bands in some of these conditions. The formation of PLC bands causes undesirable roughness on the surface, especially during deformation of large parts. It is an undesirable situation in terms of the service life of the part and the formation of cracks. In addition, the appearance of the PLC is considered a warning for the negative strain sensitivity, and the negative strain sensitivity is an undesirable condition that causes premature delivery during production. These results about PLC on dual-phase steels required more experiments

and comments. These studies can be considered as preliminary results for future works.

4.1.2. DIC Results of DP800

DIC analysis results are given with the help of photographs taken while the DP800 steel is tensile tested at given strain rate and temperature. These images were taken from the measurement region of the samples, and the scanned area is approximately 12 mm². Images of DIC experiments (Fig. 4.8-11), and strain stress curves (Fig. 4.12) are given below. The given stress-strain graphs belong to DIC tested samples.

To compare the samples, the photographs were selected at the same strain values. The scale bars represent the strain amount accumulate in the samples. For some samples more photographs were selected since the DSA phenomenon is an important issue at those parameters.

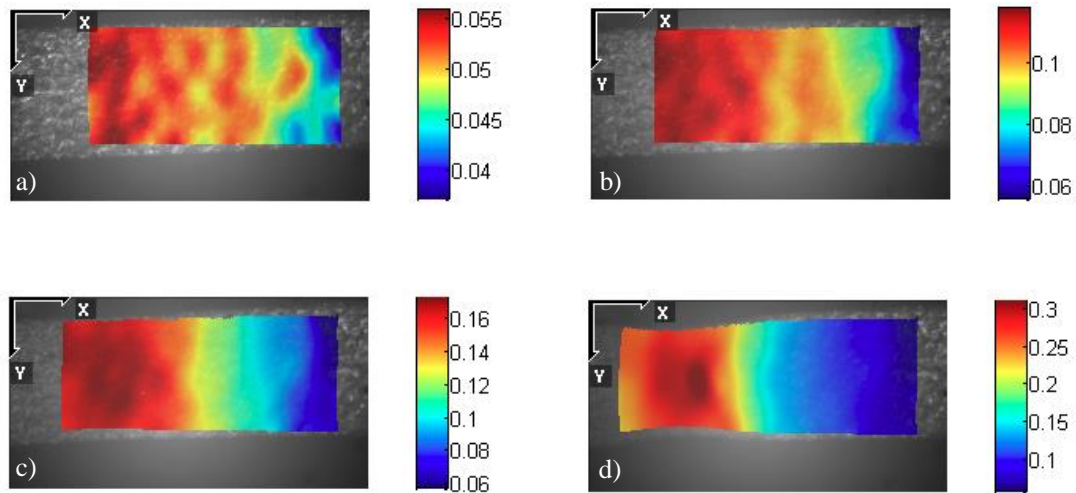


Figure 4.8 DP800 RT 10^{-3} s^{-1} ; a)5%, b)10%, c)13% [before neck], d)14% neck strain, DIC analysis

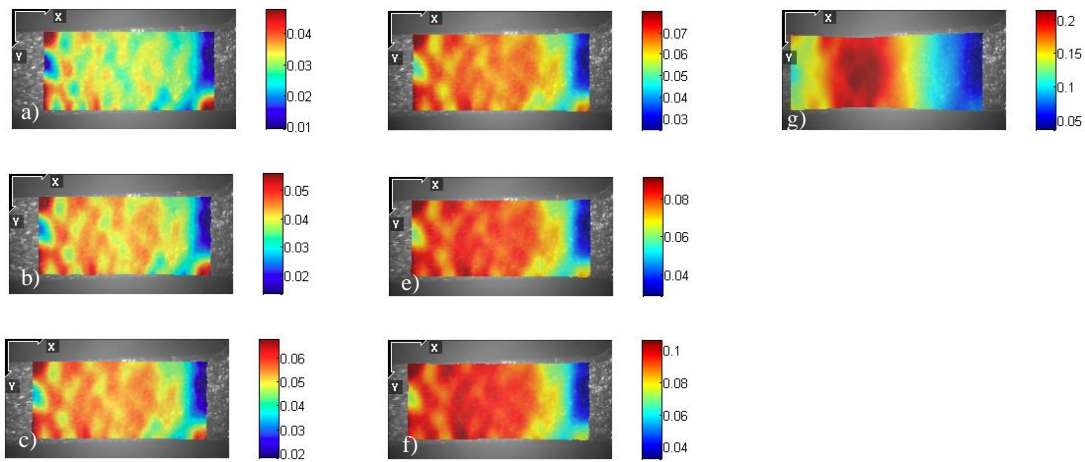


Figure 4.9 DP800 RT 1 s^{-1} ; a)3%, b)4%, c)5.2%, d)6.45%, e)7.8%, f)9.2%, g)14.6% (neck) strain, DIC analysis

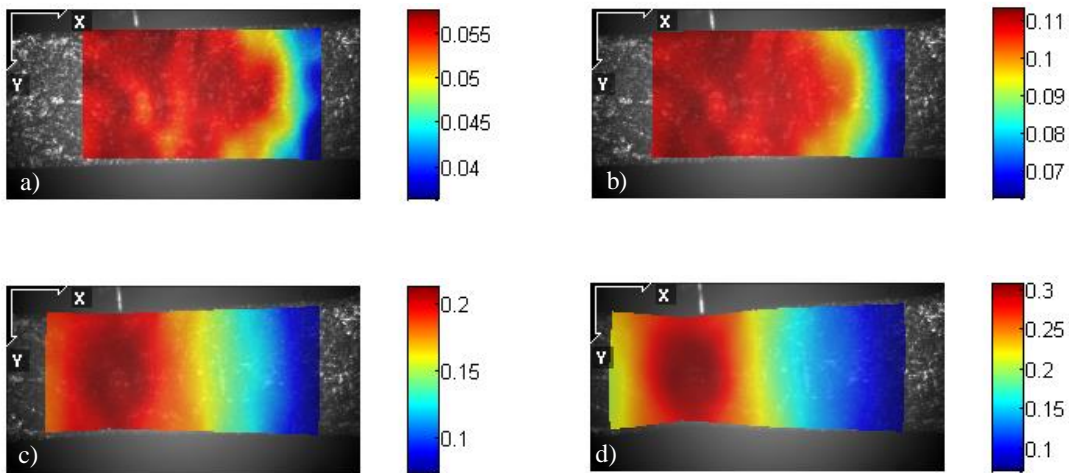


Figure 4.10 DP800 200°C 10^{-3} s^{-1} ; a)5%, b)10%, c) 17%, d)20% strain, DIC analysis

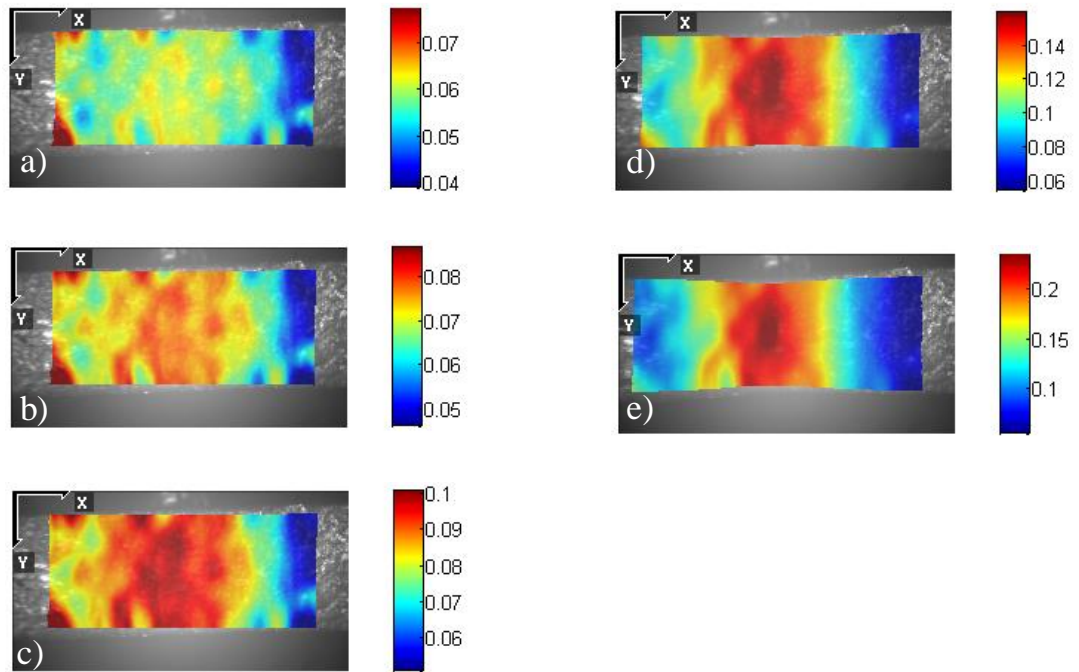


Figure 4.11 DP800 200°C 1 s⁻¹; a)3%, b)4%, c)5.2%, d)6.45%, e)7.8% strain, DIC analysis

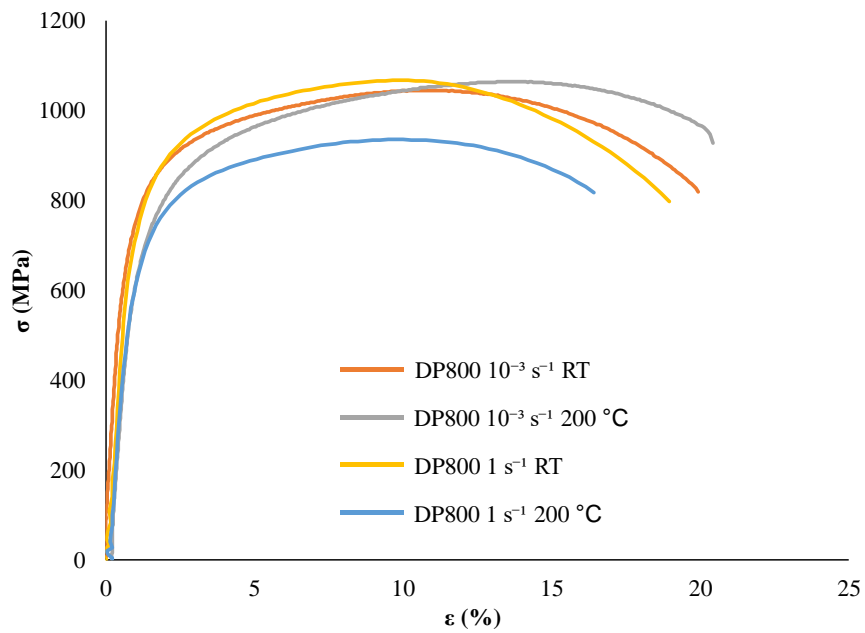


Figure 4.12 Stress&Strain curves of the DIC analyzed DP800 samples observed from tensile tests

When the DIC images obtained from figure 4.8 and 4.9 are compared, the effect of strain rate on room temperature can be seen. In this case, it is seen that there is a strain localization in certain regions, which is another indication of the flow instabilities at high strain rates.

When the images obtained from figures 4.10 and 4.11 are compared, it can be said that the temperature is not the only factor causing flow instabilities and the main factor is the strain rate.

Furthermore, since DP590 steel tests are more clear about DSA and PLC bands comment and also it is known that DP got more damage during deformation, there is no further studies shown as the cause.

Results of DIC analysis DP590 and DP800 were discussed in this section. As a result of these experiments, strain localizations are observed in certain parameters. DIC images were examined during the experiment, and it is concluded that initially, the strain is gaining as expected; however, with increasing temperature and strain rate strain fluctuations become visible.

Macro DIC experiments for DP590 steel showed significant banding, especially under conditions where the DSA mechanism considered as a dominant factor in deformation. These bands were interpreted as Portvein Le-Chatelier (PLC) bands, which is one of the significant indicators of DSA behavior on the macro scale.

4.2. Fracture Analysis of DP Steels

Fracture surface investigation studies were done to the samples which tensile tested at dilatometer for DIC analysis. For DP590 steel, the DSA behavior is more dominant so, the fracture surface of more samples was examined for DP590.

In order to perform the fracture analysis properly, the broken surface is not touched or the broken parts are not brought back together. However, the samples were cleaned by ultrasonic cleaning to ensure that there were no residues on the surface.

4.2.1. Fracture Analysis of DP590

As mentioned more fracture analysis was done on the DP590. The images taken with the help of scanning electron microscope (SEM) are given below (Fig. 4.13-16).

Fig. 4.13 (a) is the SEM image of DP590 steel, which was tensile tested at room temperature at a strain rate of 10^{-3} s^{-1} . Figure 4.13 (b) shows the image taken from the fracture surface of DP590 steel, which was tested at 200° C at 10^{-3} s^{-1} .

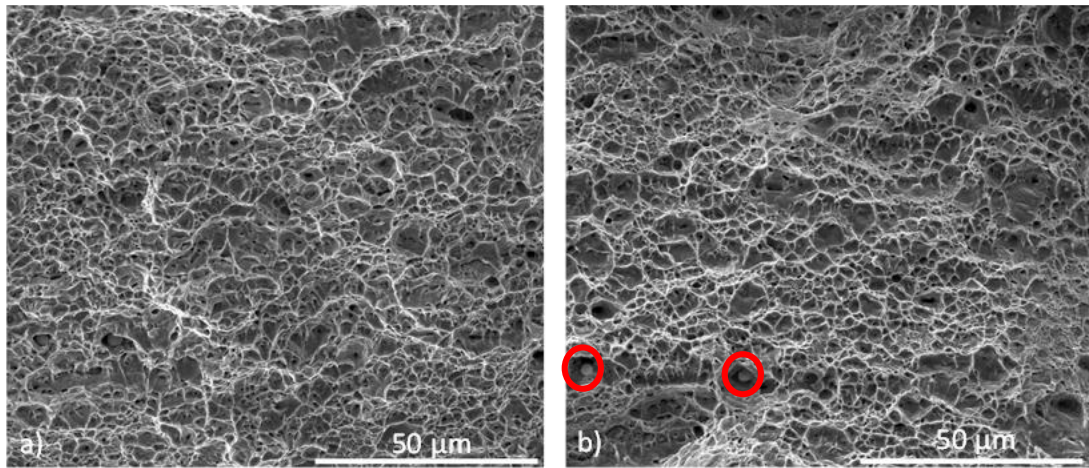


Figure 4.13 Fracture surface of DP590 10^{-3} s^{-1} ; a)RT, b)200 °C (red circles shows the nucleation cites)

When the fracture surface of these two conditions DP590 steel were examined, as expected, they exhibit ductile fracture behavior. These photos were taken at the same magnification. Since the only difference in these two rises from the temperature, as

seen the dimples are larger in high temperatures and also since these samples tested at low strain rate no visible DSA effect was observed at the fracture surface images.

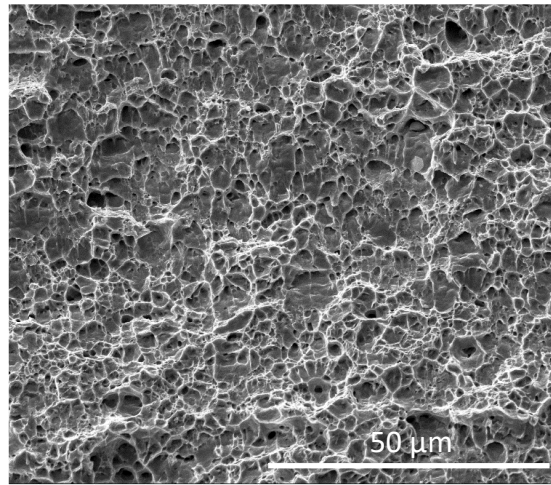


Figure 4.14 Fracture surface of DP590 1 s^{-1} RT

Figure 4.14, the SEM image of DP590 steel, which was tensile tested at room temperature at a strain rate of 1 s^{-1} is given. When this figure is compared with the Fig. 4.13 it can be concluded that the dimples and the whole fracture surface seem more homogeneous at the low strain rate and temperature, and also, the dimples seem larger at the high temperature.

Figures 4.15. a), b), c), d) are images taken from fracture surfaces of DP590 steel samples after tensile tested at $200 \text{ }^\circ\text{C}$ at strain rate 1 s^{-1} . Many images are taken at different magnifications since these are the parameters that abnormal deformation

behavior with the DSA mechanism observed. Therefore, in those images, differences of dimples, pores, propagation of crack etc. expected to be seen.

When the images of DP590 obtained from different parameters are analyzed, it is understood from the fracture surfaces the steel is failed in the ductile type of fraction. Dimples are the most characteristic features of this type of fraction.

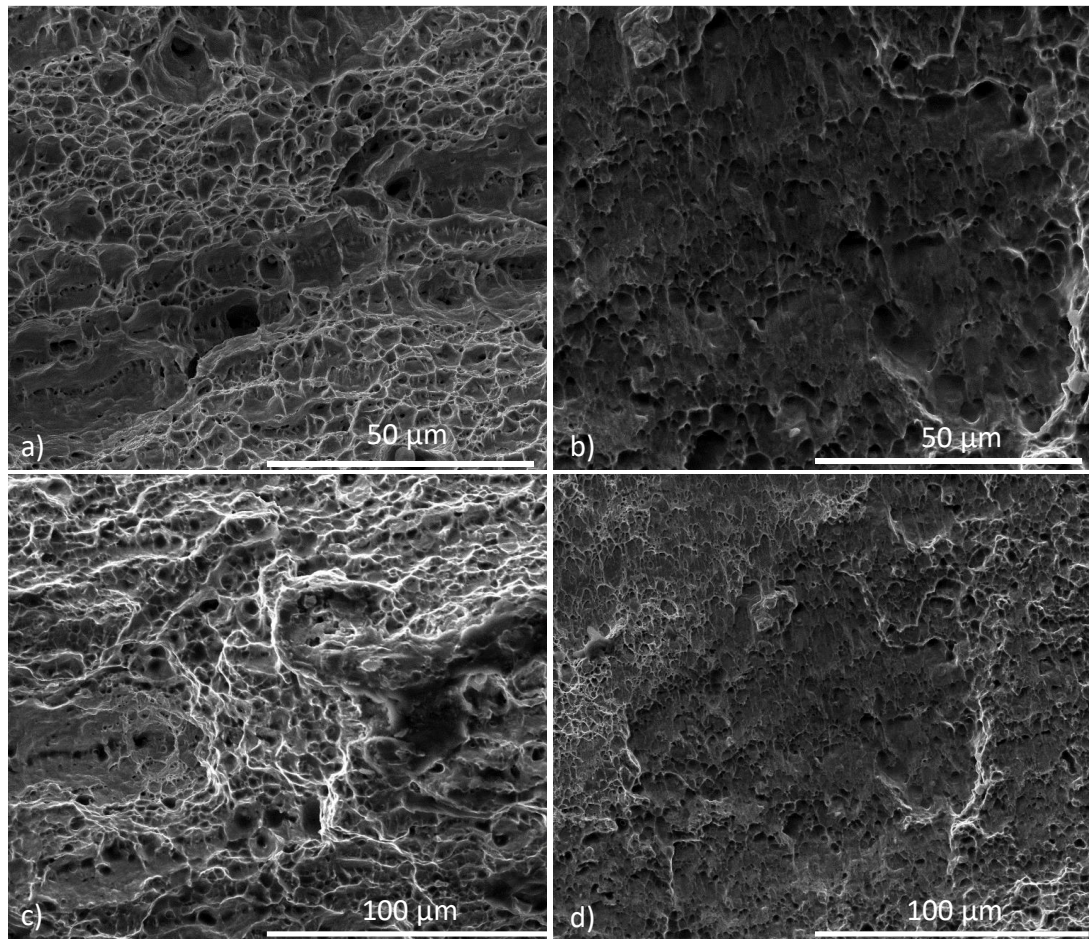


Figure 4.15 Fracture surface of DP590 1 s^{-1} 200 °C; a)3000x, b)3000x, c)1600x, d)1500x

In figure 4.15, it is seen that there are dimples in Fig. 4.15 a) & c) and shear dimples in Fig. 4.15 c) & d). The appearance of these shear dimples is due to the change of

orientation of the dimples in that direction. This may be stated as another indicator of expected and observed flow instabilities behavior at high tensile speeds.

Figures 4.14 and 4.15 are the experiments which were conducted at the same strain rate but at different temperatures. Therefore, when these images are compared, it is seen that the dimensions of the dimples are increasing with increasing temperature. Also, at the high temperatures and high strain rate, shear dimples are widely seen in the SEM images. When high-scale images are examined in the obtained images, it is observed that pore is formed in the sample and dispersed in line. These pores are the ones that coalesce, form a crack and then cause a rupture.

The inclusions marked with red circles in Fig. 4.13b as an example, are the particles that serve as void nucleation sites that cause fracture after coalescence and form a crack. The void formation starts around the inclusion which is immobile during the tensile test, and so that when the material elongates, the inclusions are also elongate and spread. In this case, the voids formed by other inclusions and also elongated and all these are connecting at some point then propagate until the tearing of the material occurs.

To conclude, the variation of the fracture surface images of DP590 steel taken at the different conditions tried to examine. In the low strain rate and RT condition, a more homogeneous dimple structure is seen. Meanwhile, when the strain rate and temperature of the test changed, observed images also evolved, such as homogeneity of the dimples and appearance of the shear dimples. Due to the characteristic structure of the DP590, there is no doubt that the fracture type is ductile whatever the tested parameter is. On the other hand, the size and orientation of the dimples show significant differences. This can be related to the flow instabilities during deformation in the material with increasing temperature and strain rate.

4.2.2. Fracture Analysis of DP800

As explained only a few fracture surface analyses are done at the DP800 steel. When the SEM images obtained from DP800 steel are examined, the dimples which are

characteristic features of the ductile type of fracture are seen in the figure 4.16 and figure 4.17.

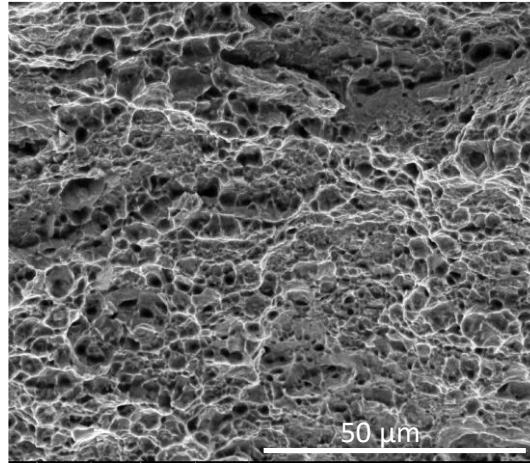


Figure 4.16 Fracture surface of DP800 10^{-3} s^{-1} RT

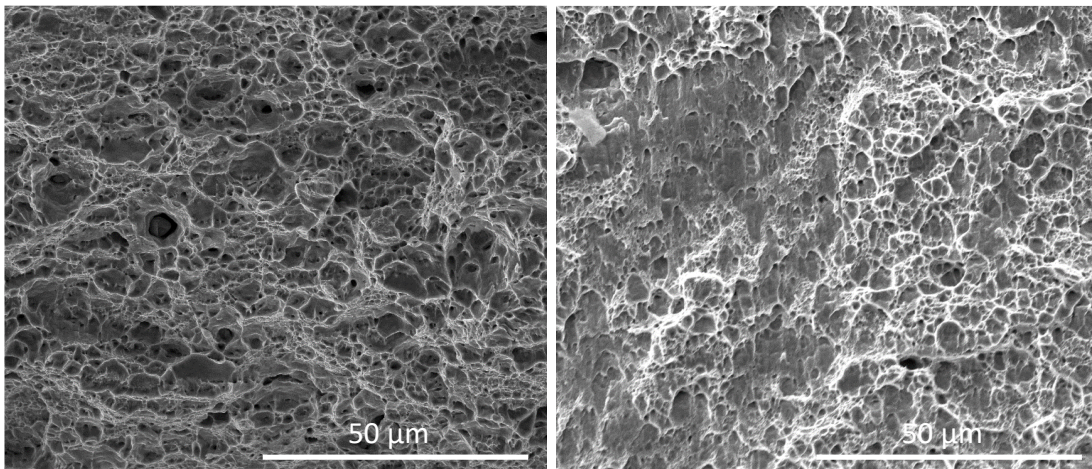


Figure 4.17 Fracture surface of DP800 1 s^{-1} RT

DSA mechanism is more effective in DP590 and that grade got more damage during deformation as stated in many ways in this thesis. Although this DP590 fact, the fracture surfaces of DP800 samples are also examined. Shear dimples are also seen in

figure 4.17a., and the dimples are again not homogeneously distributed as expected from the high strain rate experiments. Likewise, inclusion residues that cause dimple formation on these fracture surfaces are also seen in SEM photographs.

4.3. Damage Parameter Evolution with Temperature and Strain Rate

Evaluated damage values are given in Table 4.1-6 with the elastic modulus values and also damage parameter vs. strain graphs of DP590 are given in Figure 4.18 for various strain rates and temperatures. As expected, damage values increase with increasing strain at every temperature and strain rate. However, the rate of increase changes, as the damage rapidly increases until 2% strain ($\Delta D/\Delta \epsilon = 0.0173$), followed by a smooth and steady increase between 2% and 16% strain ($\Delta D/\Delta \epsilon = 0.0020$). This trend is also similar for all the tested temperatures and strain rates. After 16% strain, a local neck develops in the samples, preventing accurate measurements of the damage parameter. Under constant strain and strain rate (10^{-3} s^{-1}), damage significantly increases when the temperatures are increased to the warm forming conditions (200 – 300 °C) (Fig.4.18). At the low strain rates, the highest damage values are observed at 200 °C, whereas the lowest are at the room temperature. The differences between the highest and the lowest damage value are almost: 7X for 2% strain, 2.7X for 8% strain and 2X for 16% strain. These results indicate a significant negative impact of temperature on the damage evolution. Between 200 – 300 °C, DSA is active in DP steels and it is the likely mechanism responsible from the damage increase at constant strain. The previous results in literature have showed that the DSA is more dominant in DP590 at 200 °C compared to 300 °C [8], confirming the observed damage behavior. Nevertheless, the damage is still significantly higher at 300 °C compared to the room temperature, suggesting that the DSA is dangerous at any extent. This kind of increase in damage with temperature has never been reported in the literature. Only comparable experimental data in the literature is ~ 0.008 for DP600 deformed parallel to its rolling direction at 6% strain, room temperature and low strain rate [57]. This value increases

to ~ 0.018 when the testing direction is perpendicular to the rolling direction [20], meanwhile the damage value in our study is 0.018 for DP590 tested at 8% strain, 10^{-3} s^{-1} strain rate, and room temperature. There are no studies in the literature that are performed in the DSA range. While the exact micro-mechanisms of damage evolution are unknown under DSA, it is clear that the DSA increases void fraction and thereby reduces the elastic modulus.

At a given strain and temperature, damage further increases as the strain rate approaches to the forming relevant conditions (10 s^{-1}). The increases are most prominent for the room temperature results: 5.2X for 2% strain, 2.3X for 8% strain and 1.8X for 16% strain (Fig. 4.18). Here, the high strain rate may have caused an adiabatic temperature rise in the samples due to the deformation heating and this may be responsible from the significant damage increase in the room temperature tests. However, the high strain rate still worsens the damage behavior at the high temperatures, where the increases are almost similar at all strain levels: 1.2X at 200 °C and 2X at 300 °C compared to the low strain rate tests. At high strain rates, the damage values are always higher at 300 °C compared to the 200 °C results. Among all the experiments performed on DP590, the highest recorded damage value is 0.08 at 300 °C, 10 s^{-1} strain rate, 16% strain. The results from high strain rate experiments confirm the importance of strain rate in controlling the damage behavior in addition to the temperature. The previous results in the literature showed that the high strain rates (> 1 s^{-1}) increases the DSA activity. The DSA, in this case, may be again responsible from the damage increase. Irrespective of the micro-mechanisms behind the damage evolution, the increase in strain rate is as dangerous as the temperature rise. High strain rates are easily accessible even at room temperature forming processes, and a damage increase of 5X is possible at low strains.

Table 4.1 Damage parameter and E modulus values of DP590 at RT and 10^{-3} s^{-1}

<i>Strain (%)</i>	0	1	2	8	16
<i>Ave. E (GPa)</i>	206.00	205.80±0.5	204.98±0.5	202.25±0.86	200.046±1.1
<i>Damage P.</i>	0	0.001	0.005	0.018	0.029
<i>Std. dev</i>	---	0.0012	0.0020	0.0023	0.0026

Table 4.2 Damage parameter and E modulus values of DP590 at 200° C and 10^{-3} s^{-1}

<i>Strain (%)</i>	0	1	2	8	16
<i>Ave. E (GPa)</i>	206.00	202.63±0.43	198.88±1.6	196.18±1.12	193.27±1.16
<i>Damage P.</i>	0	0.016	0.035	0.048	0.062
<i>Std. dev</i>	---	0.0014	0.0034	0.0024	0.0026

Table 4.3 Damage parameter and E modulus values of DP590 at 300° C and 10^{-3} s^{-1}

<i>Strain (%)</i>	0	1	2	8	16
<i>Ave. E (GPa)</i>	206.00	203.04±0.8	201.78±0.71	196.74±1.1	195.55±1.68
<i>Damage P.</i>	0	0.014	0.021	0.045	0.051
<i>Std. dev</i>	---	0.0023	0.0012	0.0026	0.0038

Table 4.4 Damage parameter and E modulus values of DP590 at RT and 10 s⁻¹

<i>Strain (%)</i>	0	1	2	8	16
<i>Ave. E (GPa)</i>	206.00	204.17±0.79	200.60±1.31	197.48±0.96	195.05±1.25
<i>Damage P.</i>	0	0.009	0.026	0.041	0.053
<i>Std. dev</i>	---	0.0018	0.0034	0.0027	0.0032

Table 4.5 Damage parameter and E modulus values of DP590 at 200° C and 10 s⁻¹

<i>Strain (%)</i>	0	1	2	8	16
<i>Ave. E (GPa)</i>	206.00	199.26±0.94	197.81±1.25	195.34±1.22	190.62±1.17
<i>Damage P.</i>	0	0.033	0.040	0.052	0.075
<i>Std. dev</i>	---	0.0020	0.0028	0.0027	0.0025

Table 4.6 Damage parameter and E modulus values of DP590 at 300° C and 10 s⁻¹

<i>Strain (%)</i>	0	1	2	8	16
<i>Ave. E (GPa)</i>	206.00	198.90±1.12	197.44±1.42	193.31±1.32	189.23±1.52
<i>Damage P.</i>	0	0.035	0.042	0.062	0.081
<i>Std. dev</i>	---	0.0017	0.0030	0.0028	0.0041

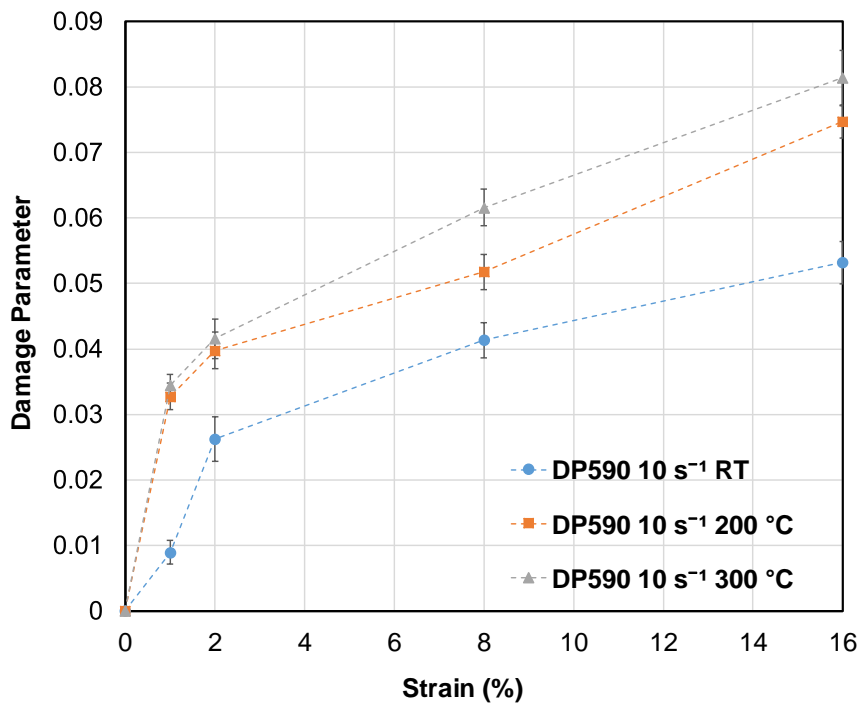
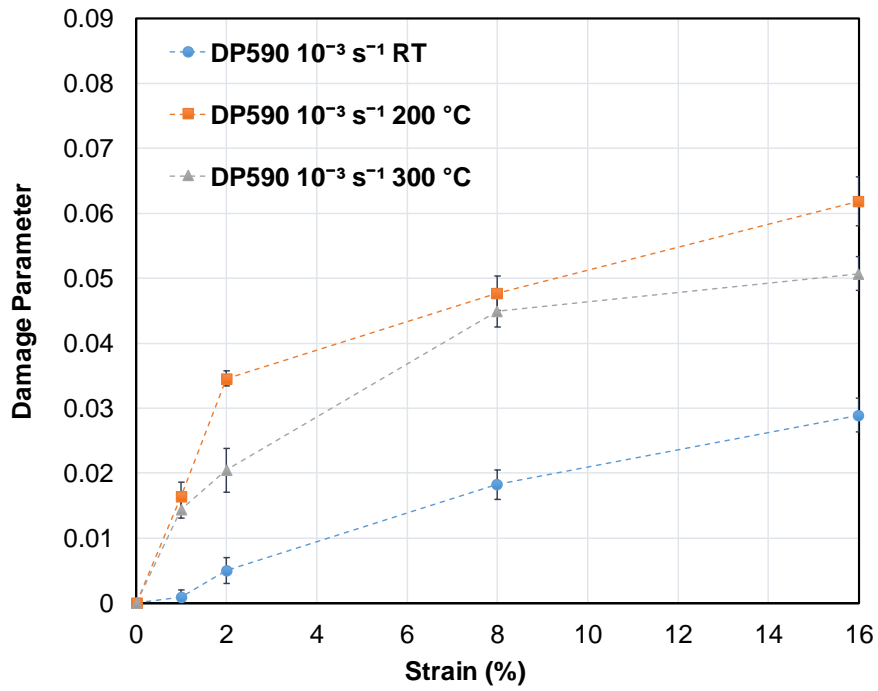


Figure 4.18 Damage parameter vs. strain graphs of DP590 tested at different temperatures; (top) low strain rate, 10⁻³ s⁻¹ vs (bottom) high strain rate, 10 s⁻¹.

Figure 4.19 shows the damage parameter vs. strain graphs of DP800 and the exact data also tabulated at the Table 4.7-12. The damage increases with strain at all temperatures and strain rates. Similar to the DP590, the damage increase can be divided into two regions, where $\Delta D/\Delta \epsilon \approx 0.0104$ for 0 – 2% strain and $\Delta D/\Delta \epsilon \approx 0.0026$ for 2 – 10% strain. Tensile tests were conducted until 10% strain for DP800 as the samples developed a local neck after 10% strain. At low strain rates (10^{-3} s^{-1}), damage evolution is less sensitive to the temperature in DP800 and the highest damage values are always observed at 300 °C. The differences between the highest and the lowest damage values are almost: 1.5X for 2% strain, 1.3X for 6% strain and 1.7X for 10% strain. The strain rate, on the other hand, has a more pronounced effect on the damage evolution in DP800. For the room temperature tests, 10 s^{-1} strain rate increases damage by: 1.6X for 2% strain, 1.3X for 6% strain and 1.4X for 10% strain (Fig.4.19). For 200 and 300 °C, damage increases are similar and the average values are: 2X for 2% strain, 1.5X for 6% strain and 1.4X for 10% strain when compared to the 10^{-3} s^{-1} strain rate tests (Fig.4.19). Among all the experiments performed on DP800, the highest recorded damage value is 0.072 at 300 °C, 10 s^{-1} strain rate, 10% strain. This value is smaller compared to the maximum damage in DP590, but it is obtained at a lower strain. At constant strain (2%), strain rate (10 s^{-1}) and temperature (300 °C), the damage in DP800 is higher than DP590 (0.046 vs 0.042), as expected from its higher martensite fraction. At higher strains and lower temperatures, on the other hand, damage in DP590 can be higher than (0.041 at 6% strain - actual 7%, RT) than the damage in DP800 (0.037 at 8% strain - actual 7.5%, RT), leading inconclusive results on damage evolution with respect to the phase fractions in DP steels.

Table 4.7 Damage parameter and E modulus values of DP800 at RT and 10^{-3} s^{-1}

<i>Strain (%)</i>	0	1	2	8	16
<i>Ave. E (GPa)</i>	210.10	208.95±0.73	206.69±0.7	204.09±1.68	203.63±0.80
<i>Damage P.</i>	0	0.005	0.016	0.029	0.031
<i>Std. dev</i>	---	0.0022	0.0018	0.0036	0.0016

Table 4.8 Damage parameter and E modulus values of DP800 at 200° C and 10^{-3} s^{-1}

<i>Strain (%)</i>	0	1	2	8	16
<i>Ave. E (GPa)</i>	210.10	207.71±0.5	205.92±1.40	203.03±1.37	200.55±1.15
<i>Damage P.</i>	0	0.011	0.020	0.034	0.045
<i>Std. dev</i>	---	0.0015	0.0032	0.0029	0.0032

Table 4.9 Damage parameter and E modulus values of DP800 at 300° C and 10^{-3} s^{-1}

<i>Strain (%)</i>	0	1	2	8	16
<i>Ave. E (GPa)</i>	210.10	207.25±1.1	205.10±1.3	201.98±1.8	198.87±1
<i>Damage P.</i>	0	0.014	0.024	0.039	0.053
<i>Std. dev</i>	---	0.0021	0.0029	0.0039	0.0028

Table 4.10 Damage parameter and E modulus values of DP800 at RT and 10 s^{-1}

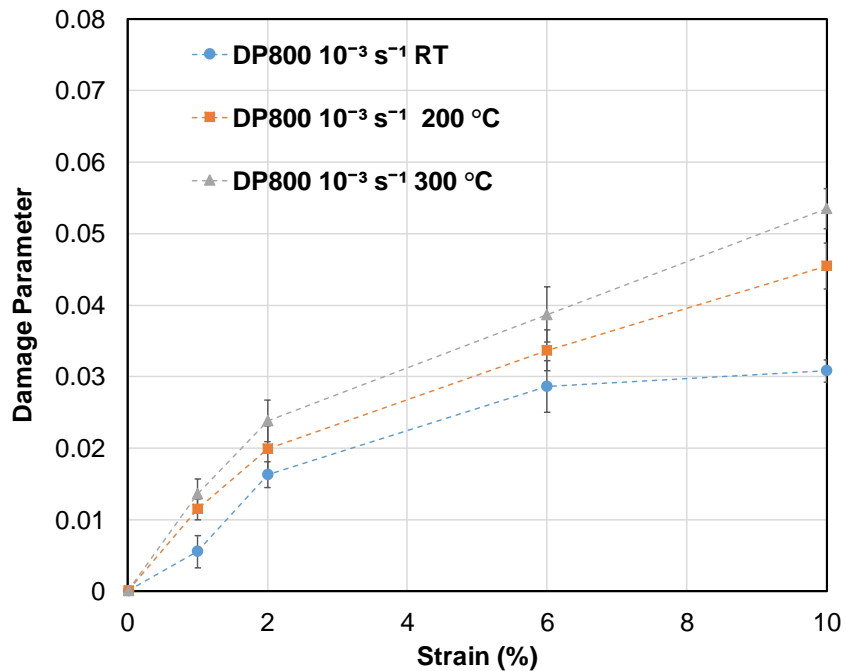
<i>Strain (%)</i>	0	1	2	8	16
<i>Ave. E (GPa)</i>	210.10	207.50±1	204.77±0.5	202.42±1.62	201.17±1.13
<i>Damage P.</i>	0	0.012	0.025	0.037	0.043
<i>Std. dev</i>	---	0.0027	0.0015	0.0034	0.0022

Table 4.11 Damage parameter and E modulus values of DP800 at 200° C and 10 s⁻¹

<i>Strain (%)</i>	0	1	2	8	16
<i>Ave. E (GPa)</i>	210.10	203.22±1	202.01±1.34	200.20±1.8	197.86±1.4
<i>Damage P.</i>	0	0.033	0.039	0.047	0.058
<i>Std. dev</i>	---	0.0020	0.0027	0.0043	0.0036

Table 4.12 Damage parameter and E modulus values of DP800 at 300° C and 10 s⁻¹

<i>Strain (%)</i>	0	1	2	8	16
<i>Ave. E (GPa)</i>	210.10	203.07±0.4	200.41±0.54	196.33±2.2	194.95±1
<i>Damage P.</i>	0	0.033	0.046	0.066	0.072
<i>Std. dev</i>	---	0.0011	0.0014	0.0048	0.0024



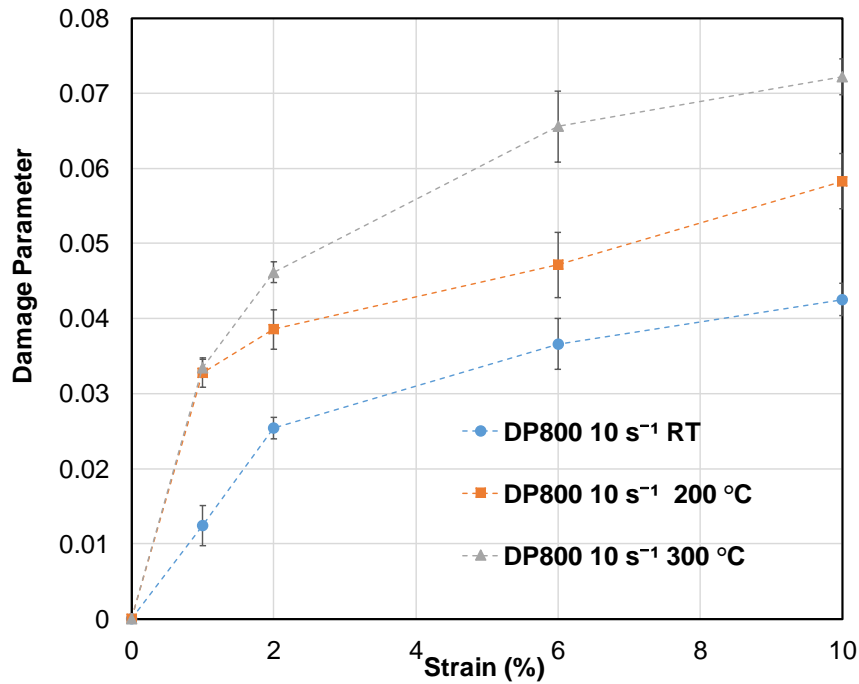


Figure 4.19 Damage parameter vs. strain graphs of DP800 tested at different temperatures; (top) low strain rate, 10⁻³ s⁻¹ vs (bottom) high strain rate, 10 s⁻¹.

Figure 4.20 summarizes the damage evolution in DP590 and DP800 steels at their uniform strains. The increase in damage with temperature and strain rate is clear for both steels. The damage linearly increases with temperature in both grades, with an exception of the peak observed in DP590 at 200 °C and 10⁻³ s⁻¹ strain rate. At all temperatures and in both grades, strain rate also increases damage. As the uniform strains are different in each grade, it is not possible to compare the absolute values of damage parameter for each grade and reach conclusions on the effects of phase fractions on the damage evolution.

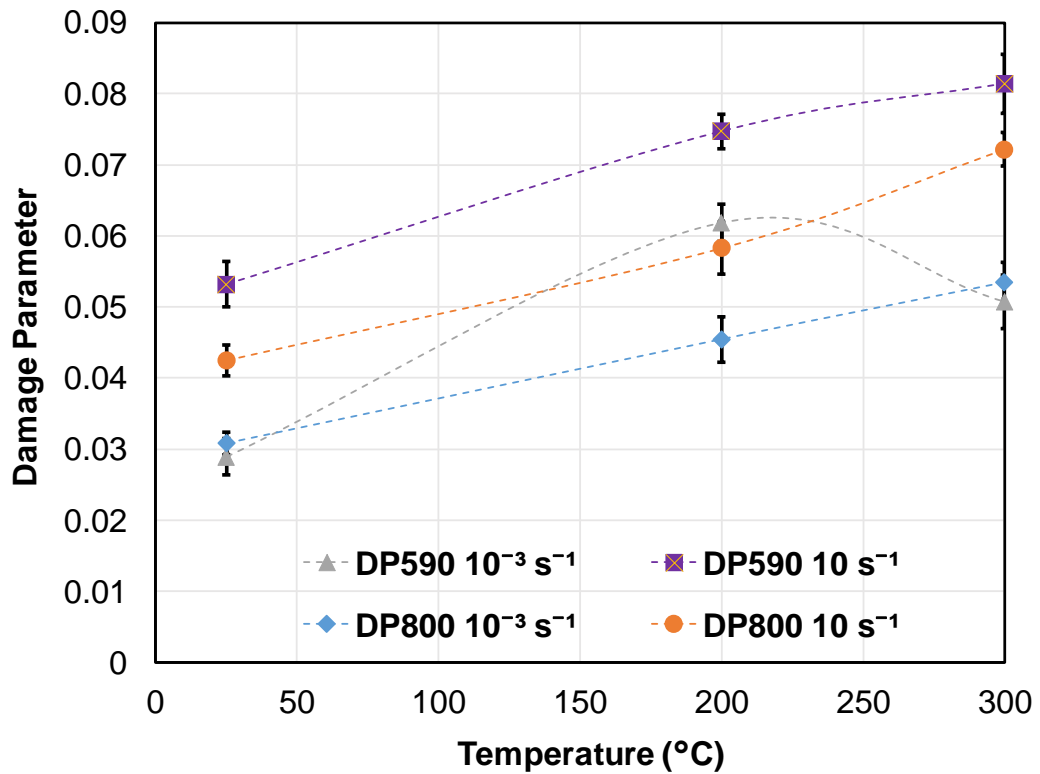


Figure 4.20 Damage parameter vs. temperature graph of DP590 and DP800 at 10^{-3} s^{-1} and 10 s^{-1} strain rates, and at their uniform strains (16% and 10%).

4.4. Microstructural Analysis of Damage

The purpose of the microstructure analysis was two folds. First, the location, shape and distribution of voids were visualized within the microstructure. For this, samples with low, intermediate, and high damage parameters were selected under constant strain for each grade. Representative and etched images with same magnification are presented in this part. Second, void fractions were measured and compared with the elastic modulus measurements (damage parameter values) in order to test the validity of the results presented in the previous section. The results are tabulated in Table 4.13, without presenting the as-polished images used for void fraction measurements.

In the DP590 sample with low damage ($D = 0.029$), a single, round void is visible at the center of the image (Fig. 4.21a). This void is within a single ferrite island and it is surrounded by the martensite phase distributed along the ferrite boundaries. In the sample with intermediate damage ($D = 0.041$), the void gets bigger and is located at the interface of two ferrite grains. An additional void also appears in another ferrite grain (Fig. 4.21b). The void gets significantly bigger as the damage increases ($D = 0.081$) and it spans among multiple ferrite islands with an irregular shape (Fig. 4.21c). In addition to the large void, multiple round and small voids exist within the ferrite islands (shown by white arrow in Fig. 4.21c). Coalescence of these small voids may have resulted in the large void that occurs at the high strain rates and temperatures, where the DSA activity may have promoted the formation of small voids within ferrite. When the void fractions are compared, sample with the smaller damage parameter has smaller void fraction and size (Table 4.13). The void volume fractions from the SEM pictures are remarkably close to the damage parameter values measured from the elastic moduli, indicating the validity of these measurements.

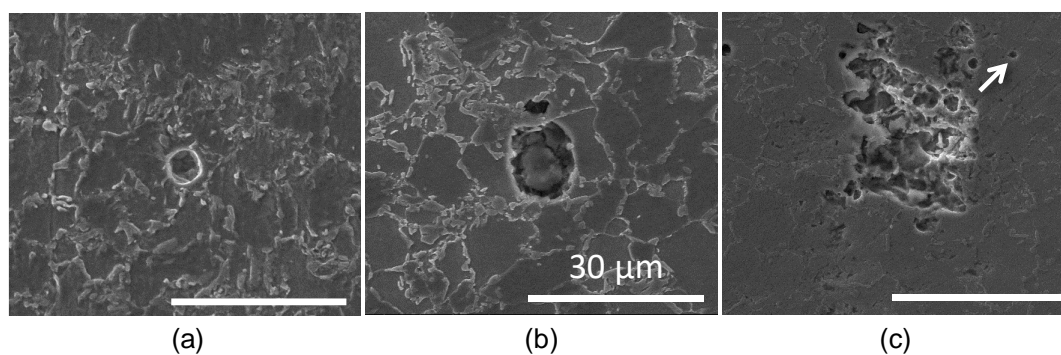


Figure 4.21 SEM pictures of DP590 tested at; a) 10^{-3} s^{-1} - RT, b) 10 s^{-1} - RT, c) 10 s^{-1} - $300 \text{ }^{\circ}\text{C}$, and at same strain of 16 %. Scale bars are $30 \text{ }\mu\text{m}$.

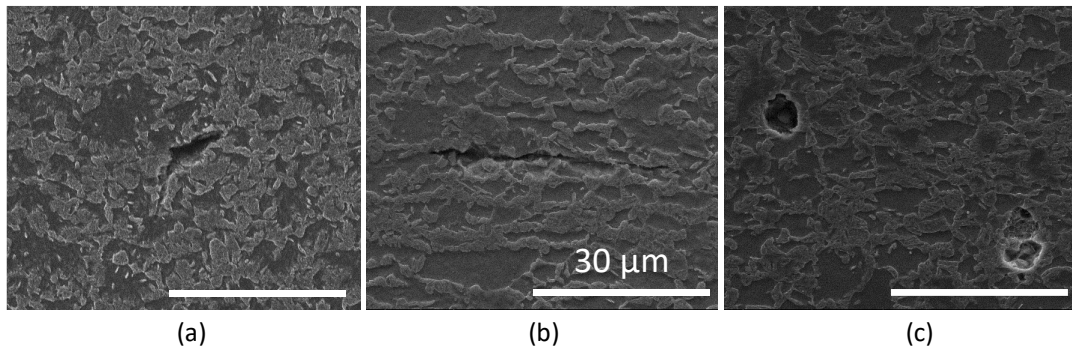


Figure 4.22 SEM pictures of DP800 tested at; a) 10^{-3} s $^{-1}$ - RT, b) 10 s $^{-1}$ - RT, c) 10 s $^{-1}$ - 300 °C, and at same strain of 10 %. Scale bars are 30 μ m.

There is again a single void existing in the representative image of DP800 sample with the low damage ($D = 0.031$) (Fig. 4.22a). In this case, the void is elongated and located at the phase boundary of martensite and ferrite. The void propagates along the phase boundaries when the strain rate, thereby damage, is increased at constant temperature ($D = 0.037$) (Fig. 4.22b). The voids get rounder, but do not get significantly bigger in DP800 as temperature increases. Due to the higher damage amount of $D = 0.072$ at this condition, fraction and number of voids rise (Fig. 4.22c). Moreover, the voids spread through the martensite and ferrite phases at the room temperature. On the other hand, they are more localized in ferrite phase as temperature increases, although voids slightly spread to martensite phase too. This may also be correlated with increasing DSA activity in ferrite at higher temperatures. Void coalescence is also visible for the bottom void in Fig. 4.22c. When the void fractions measured from SEM pictures are compared with the damage parameter values of DP800 (Table 4.13), there is again a match between two methods. The maximum deviation between two methods ($\Delta D = 0.014$) is recorded at the highest temperature and strain rate.

Table 4.13 Average void sizes and volume fractions in DP590 & DP800 obtained from SEM pictures. Damage parameters are also provided for comparison.

		<i>Average Void Size (μm)</i>	<i>Void Volume Fraction (%)</i>	<i>Damage Parameter</i>
DP590	<i>$10^{-3} \text{ s}^{-1} \text{ RT}$</i>	5.1 ± 0.4	2.32	0.029
	<i>$10 \text{ s}^{-1} \text{ RT}$</i>	6.2 ± 1.7	5.01	0.041
	<i>$10 \text{ s}^{-1} 300 \text{ }^\circ\text{C}$</i>	8.1 ± 1.0	7.02	0.081
DP800	<i>$10^{-3} \text{ s}^{-1} \text{ RT}$</i>	4.4 ± 0.7	3.06	0.031
	<i>$10 \text{ s}^{-1} \text{ RT}$</i>	4.5 ± 0.8	2.84	0.037
	<i>$10 \text{ s}^{-1} 300 \text{ }^\circ\text{C}$</i>	5.9 ± 0.6	8.62	0.072

CHAPTER 5

CONCLUSIONS AND FUTURE WORKS

5.1. Conclusions

In this thesis, DP590 and DP800 steels have been tested under different thermomechanical conditions. The tests were accompanied by strain maps obtained from DIC analysis. Results from the first part of the thesis can be summarized as follows:

- Serrations in the plastic regions of the stress-strain curves and strain localizations with banded structure are observed in some specimens. This behavior shows that the material exhibits unstable deformation behavior under certain conditions.
- Temperatures and strain rates that are relevant to the industrial deformation conditions can cause the banded strain distributions.
- PLC type bands are observed in some strain maps and the DSA is the likely mechanism causing these bands.

Moreover, the fracture surfaces of the DP steels were also investigated to get more information on the effects of DSA on the fracture behavior. Results are summarized as follows:

- Both grades exhibit the ductile type of fracture as expected.
- Dimples are observed in the SEM images which are the most characteristic features of the ductile type of fracture.
- As the strain rate and temperature increase the homogeneity of the dimples changes and also shear dimples appear.

The results from tensile tests and micro examinations show that the DSA during deformation can have negative effects. Therefore, the relationship between the DSA and damage behavior was investigated in the second part of this thesis. Results can be summarized as follows:

- In general, both DP590 and DP800 steel sheets accumulate more damage during high strain rate and high-temperature tests in contrast to low strain rate and temperature tests. Considering all strain levels, the increase in the damage is between 150%-700%. The impact of high strain rate and temperature is usually bigger for the early damage just after initial yielding ($\varepsilon = 2\%$) while still significant changes are observed up to the necking.
- When the effects of temperature and strain rate are evaluated separately, both are shown to be equally dangerous. The high strain rate alone can increase the damage by 500%. The increase in damage parameters is also confirmed by the void fraction measurements from SEM characterization.
- Aside from the fraction of voids, there are also differences between void shapes of DP590 and DP800 steels: For example, at RT, the voids are spherical and located mainly in ferrite for DP590; while the voids are elongated and span along the ferrite-martensite boundary for DP800. Moreover, increasing the strain rate seems to increase the length of the voids for DP800, whereas; the strain rate has almost no impact on spherical void morphology. Finally, temperature also influences void morphology; the voids in DP800 are no longer elongated at 300oC and 10s-1 and they become spherical and localized in ferrite. Regarding DP590, the void shape gets irregular under the same conditions with small voids also appearing in ferrite. All of those indicate that the mechanism of damage is sensitive to initial microstructure and testing conditions, from which the effect of testing conditions (temperature and strain rate) is often ignored in the study of damage.

5.2. Future Works

Recommended future works of this thesis are as follows;

- In this thesis, only macro DIC experiments were performed. Micro-DIC experiments can also be performed to obtain strain maps at the microstructural level. Therefore, DSA can be tracked at each phase separately. When DSA and PLC banding structures are examined on micro-scale useful specific results can also be obtained about individual deformation behavior of phases.
- DP steels accumulate considerable damage under the DSA conditions, yet the physical mechanism behind this behavior was not explained. In-situ tensile tests and microscopy may be necessary to explain the microstructural mechanisms.

REFERENCES

- [1] “2017 Lincoln Continental Body Structure - Boron Extrication.” [Online]. Available: www.boronextrication.com/2017/01/09/2017-lincoln-continental-body-structure/.
- [2] “2016 Honda Civic Body Structure - Boron Extrication.” [Online]. Available: www.boronextrication.com/2015/12/23/2016-honda-civic-body-structure/.
- [3] “Advanced Materials in Automotive - Advanced Manufacturing.” [Online]. Available: advancedmanufacturing.org/advanced-materials-automotive/.
- [4] “2017 Jeep Renegade Body Structure - Boron Extrication.” [Online]. Available: <http://www.boronextrication.com/2017/03/26/2017-jeep-renegade-body-structure/>.
- [5] N. Fonstein, “Dual-phase steels,” in *Automotive Steels: Design, Metallurgy, Processing and Applications*, Springer US, pp. 169–216, 2016.
- [6] H. Ghadbeigi, C. Pinna, and S. Celotto, “Failure mechanisms in DP600 steel: Initiation, evolution and fracture,” *Mater. Sci. Eng. A*, vol. 588, pp. 420–431, 2013.
- [7] Q. Lai, O. Bouaziz, M. Gouné, L. Brassart, M. Verdier, G. Parry, A. Perlade, Y. Bréchet, T. Pardoën, “Damage and fracture of dual-phase steels: Influence of martensite volume fraction,” *Mater. Sci. Eng. A*, vol. 646, pp. 322–331, 2015.
- [8] B. Bayramin, C. Şimşir, and M. Efe, “Dynamic strain aging in DP steels at forming relevant strain rates and temperatures,” *Mater. Sci. Eng. A*, vol. 704, pp. 164–172, Sep. 2017.
- [9] R. Song and Q. Dai, “Dynamic Deformation Behavior of Dual Phase Ferritic-Martensitic Steel at Strain Rates From 10^{-3} to 2000 s^{-1} ,” *J. Iron Steel Res. Int.*, vol. 20, no. 8, pp. 48–53, 2013.
- [10] R. R. U. Queiroz, F. G. G. Cunha, and B. M. Gonzalez, “Study of dynamic strain aging in dual phase steel” *Mater. Sci. Eng. A*, vol. 543, pp. 84–87, 2012.
- [11] G. Avramovic-Cingara, Y. Ososkov, M. K. Jain, and D. S. Wilkinson, “Effect of martensite distribution on damage behaviour in DP600 dual phase steels,” *Mater. Sci. Eng. A*, vol. 516, pp. 7–16, 2009.
- [12] G. Avramovic-Cingara, C. A. R. Saleh, M. K. Jain, and D. S. Wilkinson, “Void nucleation and growth in dual-phase steel 600 during uniaxial tensile testing,” *Metall. Mater. Trans. A Phys. Metall. Mater. Sci.*, vol. 40, no. 13, pp. 3117–3127, 2009.

- [13] J. Kadkhodapour, A. Butz, and S. Ziaei Rad, “Mechanisms of void formation during tensile testing in a commercial, dual-phase steel,” *Acta Mater.*, vol. 59, no. 7, pp. 2575–2588, 2011.
- [14] C. C. Tasan, M. Diehl, D. Yan, M. Bechtold, F. Roters, L. Schemmann, C. Zheng, N. Peranio, D. Ponge, M. Koyama, K. Tsuzaki, D. Raabe, “An Overview of Dual-Phase Steels: Advances in Microstructure-Oriented Processing and Micromechanically Guided Design,” *Annu. Rev. Mater. Res.*, vol. 45, no. 1, pp. 391–431, 2015.
- [15] C. Landron, O. Bouaziz, E. Maire, and J. Adrien, “Characterization and modeling of void nucleation by interface decohesion in dual phase steels,” *Scr. Mater.*, vol. 63, no. 10, pp. 973–976, 2010.
- [16] C. Landron, E. Maire, O. Bouaziz, J. Adrien, L. Lecarme, and A. Bareggi, “Validation of void growth models using X-ray microtomography characterization of damage in dual phase steels,” *Acta Mater.*, vol. 59, no. 20, pp. 7564–7573, 2011.
- [17] J. Lemaitre and R. Desmorat, *Engineering Damage Mechanics*. 94230 Cachan, France ISBN: Springer US, 2006.
- [18] R. Kuziak, R. Kawalla, and S. Waengler, “Advanced high strength steels for automotive industry: A review,” *Arch. Civ. Mech. Eng.*, vol. 8, no. 2, pp. 103–117, 2008.
- [19] C. M. Tamarelli, “AHSS 101: the evolving use of advanced high-strength steel for automotive applications, Steel Mark. Dev. Inst. 42., 2011.
- [20] J. L. K. Olsson, M. Gladh, J.E. Hedin, “Microalloyed high-strength steels,” *Adv. Mater. Process.*, vol. 8, pp. 44–46, 2006.
- [21] G. R. Speich, V. A. Demarest, and R. L. Miller, “Formation of Austenite During Intercritical Annealing of Dual-Phase Steels,” *Metall. Trans. A, Phys. Metall. Mater. Sci.*, vol. 12 A, no. 8, pp. 1419–1428, 1981.
- [22] M. S. Rashid, “Dual phase steels,” *Annu. Rev. Mater. Sci.*, no. 11:245–66, pp. 245–267, 1981.
- [23] H. C. Chen and G. H. Cheng, “Effect of martensite strength on the tensile strength of dual phase steels,” *J. Mater. Sci.*, 1989.
- [24] T. G. Koo and J. Y. Young, “On the law of mixtures in dual-phase steels,” *Metall. Mater. Trans. A Phys. Metall. Mater. Sci.*, no. 11A, pp. 852–854, 1980.
- [25] R. G. Davies, “Influence of martensite composition and content on the properties of dual phase steels,” *Metall. Mater. Trans. A Phys. Metall. Mater. Sci.*, pp. 671–679, 1978.
- [26] M. J. Molaei and A. Ekrami, “The effect of dynamic strain aging on fatigue

- properties of dual phase steels with different martensite morphology,” *Mater. Sci. Eng. A*, no. 527, pp. 235–238, 2009.
- [27] A. Das, M. Glosch, S. Tarafder, S. Sivaprasad, and D. Chakrabarti, “Micromechanisms of deformation in dual phase steels at high strain rates,” *Mater. Sci. Eng. A*, no. 680, pp. 249–258, 2017.
- [28] “Dual Phase (DP) Steels,” 2018. [Online]. Available: <https://www.worldautosteel.org/steel-basics/steel-types/dual-phase-dp-steels/>.
- [29] “Steel Your Strength,” 2018. [Online]. Available: <https://www.worldautosteel.org/why-steel/steel-your-strength/>.
- [30] R. L. Speich and G. R. Miller, “Structure and properties of dual-phase steels,” *TMS-AIME*, pp. 145–182, 1979.
- [31] R. Rana and S. B. Singh, *Automotive Steels: Design, Metallurgy, Processing and Application*. Woodhead Publishing, 2016.
- [32] S. Frechard, A. Redjaimia, and E. Lach, “Mechanical behaviour of nitrogen-alloyed austenitic stainless steel hardened by warm rolling,” *Mater. Sci. Eng. A*, no. 415, pp. 219–224, 2006.
- [33] A. Uenishi, Y. Kuriyama, H. Yoshida, and M. Takahashi, “Material characterization at high strain rates for optimizing car body structures for crash events,” *Nippon Steel Tech. Rep.*, no. 88, pp. 22–26, 2003.
- [34] D. A. Korzekwa, D. K. Matlock, and G. Krauss, “Dislocation substructure as a function of strain in a dual-phase steel,” *Metall. Trans. A*, vol. 15, no. 6, pp. 1221–1228, 1984.
- [35] A. H. Cottrell and B. A. Bilby, “Dislocation Theory of Yielding and Strain Ageing of Iron,” *Proc. Phys. Soc. Sect.*, 1949.
- [36] A. S. Key, Y. Nakada, and W. C. Leslie, “Dislocation Dynamics,” in *Dynamic strain ageing in iron and steel*, New York: Mc Graw-Hill Book Company, pp. 381–408, 1968.
- [37] J. Baird, “The effects of strain-aging due to interstitial solutes on the mechanical properties of metals,” *Met. Rev.*5, pp. 1–18, 1971.
- [38] B. Bayramin, “Dynamic Strain Aging Of Dual Phase Steels In Forming,” Middle East Technical University, 2017.
- [39] F. Ozturk, S. Toros, and S. Kilic, “Tensile and Spring-Back Behavior of DP600 Advanced High Strength Steel at Warm Temperatures,” *J. Iron Steel Res.*, pp. 41–46, 2009.
- [40] G. T. Gray, “High-Strain-Rate Deformation: Mechanical Behavior and Deformation Substructures Induced,” *Annu. Rev. Mater. Res.*, pp. 285–303,

- 2012.
- [41] A. Portvein and M. Le Chatelier, “Tensile tests of alloys undergoing transformation,” *Comptes Rendus Acad. Sci.*, pp. 507–510, 1923.
 - [42] S. J. Lee, J. Kim, S. N. Kane, and B. C. De Cooman, “On the origin of dynamic strain aging in twinning-induced plasticity steels,” *Acta Mater.*, pp. 6809–6819, 2011.
 - [43] P. Verma, G. Sudhakar Rao, P. Chellapandi, G. S. Mahobia, K. Chattopadhyay, and V. Santhi Srinivas, N.C. Singh, “Dynamic strain ageing, deformation, and fracture behavior of modified 9Cr-1Mo steel,” *Mater. Sci. Eng. A*, pp. 39–51, 2015.
 - [44] A. K. Taheri, T. M. Maccagno, and J. J. Jonas, “Effect of cooling rate after hot rolling and of multistage strain aging on the drawability of low-carbon-steel wire rod,” *Metall. Mater. Trans. A Phys. Metall. Mater. Sci.*, pp. 1183–1193, 1995.
 - [45] J. Robinson and M. Shaw, “Microstructural and mechanical influences on dynamic strain aging phenomena,” *Int. Mater. Rev.*, pp. 113–122, 1994.
 - [46] P. Rodriguez, “Serrated plastic flow,” *Bull. Mater. Sci.*, pp. 653–663, 1984.
 - [47] R. Stevenson, “Crack initiation and propagation in thermal mechanically treated sheet steels. In Formable HSLA and Dual Phase Steels,” pp. 99–108, 1979.
 - [48] M. Mazinami and W. Poole, “Effect of martensite plasticity on the deformation behavior of a low-carbon dual-phase steel,” *Metall. Mater. Trans. A Phys. Metall. Mater. Sci.*, 2007.
 - [49] G. S. C. Avramovic-Cingara and W. D. Jain MK, “Avramovic-Cingara G, Saleh CAR, Jain MK, Wilkinson DS Void nucleation and growth in dual-phase steel 600 during uniaxial tensile testing,” *Metall. Mater. Trans. A Phys. Metall. Mater. Sci.*, 2009.
 - [50] W. D. Avramovic-Cingara G, Saleh CAR, Jain MK, “Void nucleation and growth in dual-phase steel 600 during uniaxial tensile testing,” *Metall. Trans. A*, 2009.
 - [51] J. Samei, D. E. Green, J. Cheng, and M. S. de Carvalho Lima, “Influence of strain path on nucleation and growth of voids in dual phase steel sheets,” *Mater. Des.*, vol. 92, pp. 1028–1037, 2016.
 - [52] C. C. Tasan, J. P. M. Hoefnagels, M. Diehl, D. Yan, F. Roters, and D. Raabe, “Strain localization and damage in dual phase steels investigated by coupled in-situ deformation experiments and crystal plasticity simulations,” *Int. J. Plast.*, vol. 63, pp. 198–210, Dec. 2014.

- [53] A. Bareggi, E. Maire, O. Bouaziz, and M. Di Michiel, “Damage in dual phase steels and its constituents studied by X-ray tomography,” *Int. J. Fract.*, vol. 174, no. 2, pp. 217–227, 2012.
- [54] E. Maire, O. Bouaziz, M. Di Michiel, and C. Verdu, “Initiation and growth of damage in a dual-phase steel observed by X-ray microtomography,” *Acta Mater.*, vol. 56, no. 18, pp. 4954–4964, 2008.
- [55] C. C. Tasan, J. P. M. Hoefnagels, and M. G. D. Geers, “Identification of the continuum damage parameter: An experimental challenge in modeling damage evolution,” *Acta Mater.*, vol. 60, no. 8, pp. 3581–3589, 2012.
- [56] J. D. Lord and R. M. Morrell, “Elastic modulus measurement - Obtaining reliable data from the tensile test,” *Metrologia*, vol. 47, no. 2, 2010.
- [57] G. Gerstein *et al.*, “Experimental analysis of anisotropic damage in dual-phase steel by resonance measurement,” *Int. J. Damage Mech.*, vol. 26, no. 8, pp. 1147–1169, 2017.
- [58] C. C. Tasan, “Micro-mechanical Characterization of Ductile Damage in Sheet Metal,” Eindhoven University, 2010.
- [59] O. West, J. Lian, S. Münstermann, and W. Bleck, “Numerical determination of the damage parameters of a dualphase sheet steel,” *ISIJ Int.*, vol. 52, no. 4, pp. 743–752, 2012.
- [60] J. Lian, S. Münstermann, and W. Bleck, “Damage and fracture loci for a dual-phase steel and a high-strength low-alloyed steel: Revealing the different plastic localization-damage-ductile fracture pattern,” *AIP Conf. Proc.*, vol. 1769, 2016.
- [61] R. O. Santos *et al.*, “Damage identification parameters of dual-phase 600-800 steels based on experimental void analysis and finite element simulations,” *J. Mater. Res. Technol.*, no. x x, pp. 1–16, 2018.
- [62] “Gleeble user manual.” [Online]. Available: <https://www.bleedle.com/products/bleedle-systems/bleedle-3800.html>.
- [63] “ARGUS Optical Forming Analysis.” [Online]. Available: <https://www.gom.com/metrology-systems/argus.html>.
- [64] J. P. Panakkal, “Use of Longitudinal Ultrasonic Velocity as a Predictor of Elastic Moduli and Density of Sintered Uranium Dioxide,” *IEEE Trans. Ultrason. Ferroelectr. Freq. Control*, vol. 38, no. 3, pp. 161–165, 1991.
- [65] J. Hu and K. S. Raghavan, “Dynamic Strain Aging Behavior in Dual Phase and Multiphase High Strength Steels,” *IOP Conf. Ser. Mater. Sci. Eng.*, vol. 418, no. 1, 2018.

